RAA 2016 Vol. **16** No. **6**, 89 (18pp) doi: 10.1088/1674–4527/16/6/089
http://www.raa-journal.org *http://iopscience.iop.org/raa*

Research in Astronomy and Astrophysics

An H_2O Maser survey towards BGPS sources in the Outer Galaxy

Hong-Wei Xi[1,2], Jian-Jun Zhou[1,3], Jarken Esimbek[1,3], Gang Wu[1,3], Yu-Xin He[1,2], Wei-Guang Ji[1,3], Xiao-Ke Tang[1,2] and Ye Yuan[1,3]

[1] Xinjiang Astronomical Observatory, Chinese Academy of Sciences, Urumqi 830011, China; *xihongwei@xao.ac.cn*
[2] University of Chinese Academy of Sciences, Beijing 100049, China
[3] Key Laboratory of Radio Astronomy, Chinese Academy of Sciences, Urumqi 830011, China

Received 2015 May 3; accepted 2015 December 25

Abstract We performed an H_2O maser survey towards 274 Bolocam Galactic Plane Survey (BGPS) sources with $85^\circ < l < 193^\circ$ using the Nanshan 25 m radio telescope. We detected 25 H_2O masers, and five of them are new detections. The detection rate of H_2O masers in our sample is 9% which is very low. The detection rate of H_2O masers increases as the 1.1 mm flux density of BGPS sources increases, and both the peak flux density and luminosity of H_2O masers increase as the sources evolve. The detection rate of H_2O masers toward BGPS sources without HCO^+ emission is low. The BGPS sources associated with both H_2O and CH_3OH masers seem to be more compact than those only associated with H_2O masers. This indicates that the sources with both masers may be in a relatively later evolutionary stage. The strongest H_2O maser source G133.715+01.217, also well known as W3 IRS 5 which has a flux density of 2.9×10^3 Jy, was detected at eight different nearby positions. By measuring the correlation between the flux densities of these H_2O masers and their angular distance from the true source location, we get the influence radius $r = \frac{1}{0.8}\log(\frac{F_0}{3\mathrm{rms}})$. For our observations, strong sources can be detected anywhere within this radius. It is helpful to determine whether or not a weak maser nearby the strong maser is a true detection.

Key words: masers — radio lines: ISM — stars: formation

1 INTRODUCTION

Massive stars (with main sequence masses $\geqslant 8\,M_\odot$) mainly lie in the spiral arms of the Milky Way (MW). They inject significant amounts of energy into the MW, and play an important role in its evolution. They are also the main provider of ultraviolet (UV) radiation. The energetic stellar wind forms diffuse media which could form the next generation of stars (Zinneker 1990). Eventually, they form the heavy elements at the end of their life when they explode as supernovae (Kennicutt 2005). However, the formation of massive stars still remains a mystery. They are deeply embedded in the parental molecular cloud in which they formed. It is hard to observe them at optical wavelengths due to the heavy extinction. Masers associated with massive star formation could penetrate thick clouds at centimeter and millimeter wavelengths. They provide a powerful tool for investigating the dynamics and physical conditions of massive star-forming regions at very high angular resolutions (Sanna et al. 2010a,b; Moscadelli et al. 2011).

H_2O, CH_3OH and OH masers are common interstellar masers associated with a star formation region (SFR). H_2O masers are the most common maser species in our MW (Caswell 2007). They are associated with both low- and high-mass SFRs. It is widely accepted that the H_2O masers are collisionally excited by outflows or jets from an SFR. High angular resolution observations of H_2O masers (Sanna et al. 2010a,b) have been used to research the kinematic properties and to measure the magnetic strength of a molecular cloud via Zeeman splitting (Surcis et al. 2011), and to find accurate distances via their trigonometric parallax (Hachisuka et al. 2006). Hence, searching for more interstellar H_2O masers is important for the investigation of massive star formation as well as the structure of the MW.

The Bolocam Galactic Plane Survey (BGPS) (Aguirre et al. 2011) is a 1.1 mm continuum survey of 170 $\deg^2$ of the Galactic plane in the northern hemisphere with the Bolocam instrument employed at the Caltech Submillimeter Observatory (CSO). Dunham et al. (2010) suggested that BGPS sources are the cradles of high-mass stars since they contain high-mass SFRs at different evolutionary stages. BGPS sources are good targets for H_2O maser surveys.

In this paper, source selection and observation are described in Section 2. The results of observation are shown in Section 3. We also give the description for individual masers in Section 4. The discussions are given in Section 5, and the conclusions are given in Section 6.

2 SOURCE SELECTION AND OBSERVATION

The sources in our sample were selected from BGPS source catalog v1.0.1. Our aim is to to investigate the activities of star formation in BGPS sources that are located in the outer Galaxy. The BGPS sources with longitude between 85° and 194° are the main targets for our search for H_2O masers. Schlingman et al. (2011) performed observations of HCO^+ and N_2H^+ toward 1882 BGPS sources. 77% of the sources show HCO^+ emission which traces a region with high column density. Dunham (2012) conducted an H_2O maser survey towards the BGPS sources which show HCO^+ emission. We note that many of these sources are located in the outer Galaxy. First, we select sources which were not included in the observations of Schlingman et al. (2011) (67.5″, half of the Half Power Beam Width (HPBW) of the Nanshan radio telescope is used as a criterion to judge the association). As a result, we select 182 BGPS sources. Second, we select some sources from Schlingman et al. (2011) to investigate the correlation between H_2O masers and HCO^+ emission. Considering that the detection rate of H_2O masers may be very low for those BGPS sources which do not show HCO^+ emission, we randomly select 54 and 38 BGPS sources with and without HCO^+ emission. In total, there are 274 BGPS sources in our sample used for further analysis.

In Table 1, we give the name and equatorial coordinates for all the 274 BGPS sources. The detection results of HCO^+ in Schlingman et al. (2011) are also given in the table.

The coordinates of the peak 1.1 mm continuum position in the BGPS source catalog v1.0.1 are used to search for H_2O masers. The longitude of the BGPS sources in our sample ranges from 85.010° to 193.006°, while the latitude ranges from –1.466° to 4.168°. The 1.1 mm flux density of BGPS sources within an aperture of 120″ is used in this paper. It should be noted that the flux density in the version of the BGPS catalog published in the Rosolowsky et al. (2010) catalog should be multiplied by a factor of 1.5 (Aguirre et al. 2011). Hence, the flux densities of our sample range from 0.12 Jy to 59.13 Jy. The BGPS catalog v2.0 (Ginsburg et al. 2013) was released near the end of our survey. In this version, Ginsburg et al. (2013) performed a re-reduction of the original BGPS and gave more precise parameters (coordinates and flux density) for the objects. The latest version of the BGPS catalog is v2.1. The limited observation time did not allow us to re-observe our sources with new coordinates in v2.1. So, it is necessary to compare the parameters of our sample with those of their counterparts in v2.1; for further details see Section 5.2.

The Nanshan 25 m radio telescope, employed by Xinjiang Astronomical Observatory, was used for a 22 GHz H_2O maser survey towards the sources in our sample from September 2012 to August 2013. It has an HPBW of 135″ at 22 GHz, and its pointing accuracy is better than 18″. The telescope is equipped with one dual circular polarization (left and right) cryogenic K-band receiver as the front-end and a dual input digital filter bank (DFB) system with 8192 channels as the back-end. The system temperature under good weather conditions is ∼ 50 K. The bandwidth is 64 MHz, and the corresponding velocity resolution is 0.11 km s^{-1}. The single point mode was used for the observation. The offset-points were located 10 arcmin away from the Galactic plane in the direction of the Galactic latitude of the on-points. The integration time was 360 s for each on-point and offset-point, and total integration time was 720 s for each source. All of the observations were performed in good weather and the elevation of observation was kept between 20° and 70°. The corresponding root mean square (rms) noise level was ∼ 0.36 Jy. The conversion factor between the main-beam brightness temperature and flux density was 0.091 K Jy^{-1}. A noise diode was used in the flux density calibration. The absolute error was less than 20%.

Due to the limited observation time, we did not perform on the fly (OTF) or five-point observations towards the newly detected H_2O masers. Hence, we cannot give the position for the new detection in this paper.

3 DATA REDUCTION AND RESULTS

The spectra were reduced using the GILDAS/CLASS package[1] developed at IRAM and the Observatoire de Grenoble. The two circular polarization signals were averaged for data analysis. All spectra were smoothed by averaging four consecutive channels in order to improve the signal to noise (S/N) ratio. This resulted in a velocity resolution of 0.44 km s^{-1} and an average rms of 0.17 Jy. A feature is considered to be a maser when the S/N ratio is above 3. We detected a similar maser line profile toward some sources which are closer to each other. This indicates that strong maser emission may be detected several beams away from the source. In this case, we suggest that the strongest maser is a true detection. We discuss the influence radius of a maser with given flux density in Section 5.1. As a result, we detected 25 H_2O masers. The detection rate is 9%. Five out of 25 are new detections. The results about whether a BGPS source is associated with an H_2O maser are given in Table 1, in which the observation date and rms for each source are listed as well. The parameters describing the H_2O masers are listed in Table 2 and the corresponding spectra of the H_2O masers are displayed in Figure 1. The dashed line represents the systematic velocity derived from N_2H^+ (Shirley et al. 2013) or ^{12}CO[2,3,4].

There are three H_2O masers with flux density exceeding 10^2 Jy ($H_2O-5656$ G133.715+01.217, $H_2O-5668$ G133.949+01.063 and $H_2O-5746$ G188.792+01.027). The strongest H_2O maser is $H_2O-5656$ G133.715+01.217, well known as W3 IRS 5, which has a peak flux density of 2.9×10^3 Jy.

[1] *http://www.iram.fr/IRAMFR/GILDAS/*
[2] *http://www.radioast.csdb.cn*
[3] *http://www.dlh.pmo.cas.cn*
[4] *http://www.csdb.cn*

Table 1 The parameters of BGPS sources towards which we searched for H_2O masers. Col. (1) gives the indices of BGPS sources in our survey. Col. (2) gives the names of BGPS source in version 1.0.1. The indices and BGPS source names are also used for citing the H_2O masers detected in the position. The equatorial coordinates in J2000 are given in Cols. (3) and (4). Cols. (5) to (7) show that whether there are WISE point sources, HII regions and RMS sources associated with BGPS sources. The evolutionary phases of BGPS sources are listed in Col. (8). The searching results of HCO^+ from Schlingman et al. (2011) and Shirley et al. (2013) are listed in Cols. (9) and (10), in which '-' represents no observation performed toward the BGPS source. Col. (11) shows the result of our survey of H_2O masers. The rms in each spectrum is listed in Col. (12), and the observation date is given in Col. (13).

ID	BGPS name (v1.0.1)	RA (J2000)	DEC (J2000)	WISE	HII	RMS	Phase	HCO^+ (S11)	HCO^+ (S13)	H_2O	rms Jy	date dd-mm-yyyy
(1)	(2)	(3)	(4)	(5)	(6)	(7)	(8)	(9)	(10)	(11)	(12)	(13)
H_2O–5527	G085.010−01.322	20 58 25.1	+43 44 15	N	N	N	1	-	N	N	0.16	19-03-2013
H_2O–5528	G085.012−01.324	20 58 26.0	+43 44 15	N	N	N	1	-	N	N	0.14	19-03-2013
H_2O–5529	G085.016+00.426	20 50 58.3	+44 52 09	Y	N	N	2	-	N	N	0.16	19-03-2013
H_2O–5530	G085.022−00.300	20 54 07.8	+44 24 33	N	N	N	1	-	N	N	0.15	19-03-2013
H_2O–5531	G085.030+00.362	20 51 18.0	+44 50 21	Y	N	Y	3	Y	Y	N	0.13	19-03-2013
H_2O–5532	G085.042−00.144	20 53 31.9	+44 31 29	Y	N	N	2	Y	Y	N	0.14	19-03-2013
H_2O–5533	G085.043−00.166	20 53 38.0	+44 30 43	Y	N	N	2	-	Y	N	0.13	19-03-2013
H_2O–5534	G085.046−01.136	20 57 46.0	+43 53 09	Y	N	N	2	Y	Y	N	0.14	19-03-2013
H_2O–5535	G085.049+00.448	20 50 59.9	+44 54 33	Y	N	N	2	-	N	N	0.11	19-03-2013
H_2O–5536	G085.072−01.158	20 57 57.2	+43 53 29	Y	N	N	2	-	Y	N	0.13	19-03-2013
H_2O–5537	G085.073−00.140	20 53 37.8	+44 33 06	Y	N	N	2	Y	Y	N	0.11	19-03-2013
H_2O–5538	G085.073−00.168	20 53 45.0	+44 32 02	Y	N	N	2	-	Y	N	0.11	19-03-2013
H_2O–5539	G085.078−00.132	20 53 36.6	+44 33 36	Y	N	N	2	Y	Y	N	0.10	19-03-2013
H_2O–5540	G085.111+00.462	20 51 09.6	+44 57 57	N	N	N	1	N	N	N	0.11	19-03-2013
H_2O–5541	G085.111−01.204	20 58 17.5	+43 53 30	Y	N	N	2	N	Y	N	0.16	31-03-2013
H_2O–5542	G085.120+00.474	20 51 08.1	+44 58 47	N	N	N	1	N	Y	N	0.17	31-03-2013
H_2O–5543	G085.156−01.174	20 58 19.6	+43 56 40	N	N	N	1	-	Y	N	0.14	31-03-2013
H_2O–5544	G085.206−00.134	20 54 04.8	+44 39 25	N	N	N	1	-	N	N	0.14	31-03-2013
H_2O–5545	G085.212−00.140	20 54 07.7	+44 39 27	N	N	N	1	-	N	N	0.18	31-03-2013
H_2O–5546	G085.236+00.022	20 53 31.0	+44 46 48	Y	N	N	2	Y	Y	N	0.13	24-01-2013
H_2O–5547	G085.260+00.008	20 53 39.8	+44 47 22	Y	N	N	2	Y	Y	N	0.12	24-01-2013
H_2O–5548	G085.266+00.020	20 53 38.0	+44 48 06	Y	N	N	2	Y	Y	N	0.13	24-01-2013
H_2O–5549	G085.378+00.022	20 54 01.8	+44 53 20	N	N	N	1	-	Y	N	0.10	24-01-2013
H_2O–5550	G085.385−01.466	21 00 23.3	+43 55 36	Y	N	N	2	-	N	N	0.099	24-01-2013
H_2O–5551	G085.412+00.002	20 54 14.4	+44 54 07	Y	Y	Y	3	Y	Y	Y	0.16	24-01-2013
H_2O–5552	G085.456−00.060	20 54 40.2	+44 53 45	Y	N	N	2	N	N	N	0.081	24-01-2013
H_2O–5553	G085.481−00.060	20 54 45.8	+44 54 56	Y	N	N	2	N	Y	N	0.17	23-01-2013
H_2O–5554	G085.820+00.396	20 54 01.2	+45 28 04	N	N	N	1	-	N	N	0.14	23-01-2013
H_2O–5555	G086.989+00.526	20 57 48.6	+46 26 36	Y	N	Y	3	-	N	N	0.15	23-01-2013
H_2O–5556	G088.096+00.413	21 02 33.7	+47 12 10	Y	N	N	2	-	N	Y	0.14	23-01-2013
H_2O–5557	G089.635+00.171	21 09 46.6	+48 10 50	Y	Y	Y	3	-	N	N	0.14	24-01-2013
H_2O–5558	G089.725+00.217	21 09 56.5	+48 16 40	Y	Y	N	3	-	N	N	0.13	24-01-2013
H_2O–5559	G098.856+02.932	21 40 29.6	+56 35 53	Y	Y	Y	3	-	Y	N	0.20	15-12-2012
H_2O–5560	G098.978+03.960	21 36 08.1	+57 26 48	Y	N	N	2	Y	Y	Y	0.17	15-12-2012
H_2O–5561	G099.115+03.926	21 37 03.4	+57 30 45	Y	N	N	2	Y	Y	N	0.16	15-12-2012
H_2O–5562	G099.981+04.168	21 40 42.6	+58 16 01	Y	N	N	2	Y	Y	Y	0.19	15-12-2012
H_2O–5563	G099.992+03.094	21 46 02.3	+57 27 36	N	N	N	1	-	Y	N	0.14	15-12-2012
H_2O–5564	G109.995−00.282	23 05 23.2	+59 53 58	Y	N	N	2	Y	Y	Y	0.17	15-12-2012
H_2O–5565	G109.997−00.088	23 04 47.0	+60 04 41	Y	Y	N	3	Y	Y	N	0.17	15-12-2012
H_2O–5566	G110.003+00.330	23 03 28.4	+60 27 48	Y	N	N	2	N	N	N	0.15	15-12-2012
H_2O–5567	G110.003−00.074	23 04 47.0	+60 05 36	N	N	N	1	N	N	N	0.22	23-01-2013
H_2O–5568	G110.003−00.248	23 05 20.3	+59 56 01	N	N	N	1	N	N	N	0.17	23-01-2013
H_2O–5569	G110.016+00.270	23 03 46.4	+60 24 51	Y	N	N	2	Y	Y	N	0.18	23-01-2013
H_2O–5570	G110.039−00.284	23 05 42.9	+59 54 54	Y	N	N	2	Y	Y	N	0.19	23-01-2013
H_2O–5571	G110.070−00.214	23 05 43.7	+59 59 31	N	N	N	1	N	N	N	0.19	23-01-2013
H_2O–5572	G110.073−00.088	23 05 20.5	+60 06 30	Y	N	N	2	Y	Y	N	0.15	23-01-2013
H_2O–5573	G110.087+00.126	23 04 45.6	+60 18 37	Y	N	N	2	Y	Y	N	0.099	23-01-2013
H_2O–5574	G110.087+00.084	23 04 53.7	+60 16 18	Y	N	N	2	Y	Y	N	0.11	23-01-2013
H_2O–5575	G110.105−00.030	23 05 23.6	+60 10 27	Y	N	N	2	N	N	N	0.10	23-01-2013
H_2O–5576	G110.113+00.050	23 05 11.8	+60 15 03	Y	N	Y	3	Y	Y	N	0.26	23-01-2013
H_2O–5577	G110.126+00.086	23 05 11.1	+60 17 22	Y	N	N	2	Y	Y	N	0.26	23-01-2013
H_2O–5578	G110.141+00.084	23 05 17.7	+60 17 35	N	N	N	1	N	N	N	0.23	23-01-2013
H_2O–5579	G110.156+00.238	23 04 55.0	+60 26 27	Y	N	N	2	N	N	N	0.25	23-01-2013
H_2O–5580	G110.203+00.010	23 05 59.4	+60 15 00	N	N	N	1	N	N	N	0.24	23-01-2013
H_2O–5581	G110.228+00.956	23 03 05.5	+61 07 38	Y	N	N	2	Y	Y	N	0.22	23-01-2013
H_2O–5582	G110.228+00.958	23 03 05.1	+61 07 44	N	N	N	1	Y	Y	N	0.22	23-01-2013
H_2O–5583	G110.237−00.008	23 06 18.0	+60 14 48	Y	N	N	2	N	N	N	0.26	23-01-2013
H_2O–5584	G110.251+00.032	23 06 16.6	+60 17 20	N	N	N	1	Y	Y	N	0.23	23-01-2013
H_2O–5585	G110.254−00.578	23 08 12.8	+59 43 45	Y	N	N	2	N	N	N	0.23	23-01-2013
H_2O–5586	G110.509−00.914	23 11 05.1	+59 30 57	Y	N	N	2	-	N	N	0.24	23-01-2013

Table 1 — *Continued*

ID (1)	BGPS name (v1.0.1) (2)	RA (J2000) (3)	DEC (J2000) (4)	WISE (5)	HII (6)	RMS (7)	Phase (8)	HCO^+ (S11) (9)	HCO^+ (S13) (10)	H_2O (11)	rms Jy (12)	date dd-mm-yyyy (13)
H_2O–5587	G110.516−00.884	23 11 03.3	+59 32 47	N	N	N	1	-	N	N	0.25	23-01-2013
H_2O–5588	G110.537−00.550	23 10 11.9	+59 51 47	N	N	N	1	-	N	N	0.23	23-01-2013
H_2O–5589	G110.546−00.438	23 09 55.9	+59 58 14	Y	N	N	2	-	N	N	0.21	23-01-2013
H_2O–5590	G110.609−00.892	23 11 45.1	+59 34 25	N	N	N	1	-	N	N	0.22	23-01-2013
H_2O–5591	G110.787+00.370	23 09 13.4	+60 48 32	Y	N	N	2	-	N	N	0.25	23-01-2013
H_2O–5592	G110.795+00.382	23 09 14.8	+60 49 23	Y	N	N	2	-	Y	N	0.25	23-01-2013
H_2O–5593	G110.882+00.022	23 11 01.8	+60 31 25	Y	N	N	2	-	N	N	0.21	23-01-2013
H_2O–5594	G110.893+00.560	23 09 25.8	+61 01 30	Y	N	N	2	-	N	N	0.21	23-01-2013
H_2O–5595	G110.903+00.534	23 09 35.3	+61 00 18	Y	N	N	2	-	N	N	0.18	23-01-2013
H_2O–5596	G110.983−00.982	23 14 45.6	+59 37 42	Y	N	Y	3	-	Y	N	0.19	23-01-2013
H_2O–5597	G111.082−00.976	23 15 28.8	+59 40 13	Y	N	N	2	Y	Y	N	0.23	23-01-2013
H_2O–5598	G111.156+00.580	23 11 23.2	+61 08 38	N	N	N	1	N	N	N	0.22	23-01-2013
H_2O–5599	G111.162−00.690	23 15 15.0	+59 57 57	Y	N	N	2	N	N	N	0.22	23-01-2013
H_2O–5600	G111.192−00.900	23 16 04.6	+59 46 51	Y	N	N	2	N	N	N	0.26	23-01-2013
H_2O–5601	G111.192−00.796	23 15 46.7	+59 52 40	Y	Y	Y	3	Y	Y	N	0.21	18-08-2013
H_2O–5602	G111.248+00.810	23 11 22.6	+61 23 29	N	N	N	1	N	N	N	0.16	22-01-2013
H_2O–5603	G111.278−00.746	23 16 16.5	+59 57 19	Y	N	N	2	N	N	N	0.19	22-01-2013
H_2O–5604	G111.284−00.664	23 16 05.1	+60 02 03	Y	Y	Y	3	Y	Y	N	0.18	22-01-2013
H_2O–5605	G111.302+00.808	23 11 48.1	+61 24 36	Y	N	N	2	N	N	N	0.17	22-01-2013
H_2O–5606	G111.308−00.880	23 16 52.9	+59 50 27	Y	N	N	2	N	N	N	0.16	22-01-2013
H_2O–5607	G111.382−00.662	23 16 48.7	+60 04 16	Y	N	N	2	N	N	N	0.16	23-01-2013
H_2O–5608	G111.382+00.706	23 12 44.3	+61 20 42	N	N	N	1	Y	Y	N	0.16	23-01-2013
H_2O–5609	G111.424−00.556	23 16 49.4	+60 11 06	Y	N	N	2	Y	Y	N	0.15	23-01-2013
H_2O–5610	G111.484+00.746	23 13 24.3	+61 25 12	Y	N	N	2	Y	Y	N	0.069	22-01-2013
H_2O–5611	G111.516+00.688	23 13 50.0	+61 22 40	Y	N	N	2	Y	Y	N	0.096	22-01-2013
H_2O–5612	G111.522+00.800	23 13 32.1	+61 29 03	N	N	Y	3	Y	Y	Y	0.094	22-01-2013
H_2O–5613	G111.528+00.818	23 13 31.6	+61 30 11	Y	N	N	2	Y	Y	N	0.082	22-01-2013
H_2O–5614	G111.534+00.372	23 14 55.9	+61 05 25	Y	N	N	2	Y	Y	N	0.065	22-01-2013
H_2O–5615	G111.564+00.578	23 14 32.5	+61 17 35	N	N	N	1	N	N	N	0.082	22-01-2013
H_2O–5616	G111.606+00.614	23 14 45.5	+61 20 31	Y	N	N	2	N	N	N	0.068	22-01-2013
H_2O–5617	G111.632+00.198	23 16 12.4	+60 57 49	N	N	N	1	N	N	N	0.055	22-01-2013
H_2O–5618	G111.632+00.754	23 14 32.0	+61 28 54	N	N	N	1	Y	Y	N	0.068	22-01-2013
H_2O–5619	G111.638+00.098	23 16 32.8	+60 52 21	Y	N	N	2	N	N	N	0.060	22-01-2013
H_2O–5620	G111.650+00.048	23 16 47.1	+60 49 48	Y	N	N	2	Y	Y	N	0.059	22-01-2013
H_2O–5621	G111.650+00.414	23 15 42.2	+61 10 17	Y	N	N	2	Y	Y	N	0.17	23-01-2013
H_2O–5622	G111.650+00.796	23 14 32.7	+61 31 39	Y	N	N	2	N	N	N	0.14	23-01-2013
H_2O–5623	G111.668+00.596	23 15 17.7	+61 20 52	Y	N	N	2	Y	Y	N	0.12	23-01-2013
H_2O–5624	G111.680+00.358	23 16 06.1	+61 07 48	Y	N	N	2	N	N	N	0.14	23-01-2013
H_2O–5625	G111.716+00.640	23 15 32.1	+61 24 22	N	N	N	1	N	N	N	0.13	23-01-2013
H_2O–5626	G111.716+00.658	23 15 28.8	+61 25 22	Y	N	N	2	N	N	N	0.14	23-01-2013
H_2O–5627	G111.716+00.776	23 15 07.3	+61 31 58	N	N	N	1	Y	Y	N	0.12	23-01-2013
H_2O–5628	G111.716+00.778	23 15 07.0	+61 32 05	Y	N	N	2	Y	Y	N	0.11	23-01-2013
H_2O–5629	G111.748+00.328	23 16 43.0	+61 07 35	Y	N	N	2	Y	Y	N	0.15	23-01-2013
H_2O–5630	G111.778+00.504	23 16 25.6	+61 18 06	N	N	N	1	Y	Y	N	0.18	23-01-2013
H_2O–5631	G111.796+00.462	23 16 41.5	+61 16 08	N	N	N	1	Y	Y	N	0.17	23-01-2013
H_2O–5632	G111.796+00.600	23 16 16.8	+61 23 51	N	N	N	1	Y	Y	Y	0.23	23-01-2013
H_2O–5633	G111.820+00.504	23 16 45.2	+61 19 00	N	N	N	1	N	N	N	0.21	23-01-2013
H_2O–5634	G111.876+00.818	23 16 14.9	+61 37 47	Y	Y	N	3	Y	Y	N	0.10	21-01-2013
H_2O–5635	G111.882+00.992	23 15 46.0	+61 47 39	Y	Y	Y	3	Y	Y	Y	0.11	22-01-2013
H_2O–5636	G111.936+00.638	23 17 15.6	+61 28 59	N	N	N	1	N	N	N	0.11	22-01-2013
H_2O–5637	G111.948+00.536	23 17 39.4	+61 23 31	Y	N	N	2	N	N	N	0.097	22-01-2013
H_2O–5638	G111.954+00.964	23 16 25.3	+61 47 39	N	N	N	1	N	N	N	0.097	22-01-2013
H_2O–5639	G111.983+00.774	23 17 12.9	+61 37 36	Y	N	N	2	-	N	N	0.094	22-01-2013
H_2O–5640	G132.950+00.743	02 18 10.7	+61 54 56	N	N	N	1	-	Y	N	0.11	15-12-2012
H_2O–5641	G132.965+00.739	02 18 16.8	+61 54 26	N	N	N	1	-	Y	N	0.13	15-12-2012
H_2O–5642	G133.001+00.753	02 18 36.5	+61 54 31	Y	N	N	2	-	Y	N	0.10	15-12-2012
H_2O–5643	G133.206+01.109	02 21 16.9	+62 10 30	Y	N	N	2	-	Y	N	0.17	15-12-2012
H_2O–5644	G133.408+01.181	02 23 07.1	+62 10 24	Y	N	N	2	-	Y	N	0.11	15-12-2012
H_2O–5645	G133.413+01.185	02 23 09.8	+62 10 32	Y	N	N	2	-	Y	N	0.097	15-12-2012
H_2O–5646	G133.513+00.971	02 23 19.8	+61 56 25	N	N	N	1	-	Y	N	0.090	15-12-2012
H_2O–5647	G133.555+01.003	02 23 45.5	+61 57 20	N	N	N	1	-	N	N	0.090	15-12-2012
H_2O–5648	G133.558+01.015	02 23 49.6	+61 57 56	N	N	N	1	-	N	N	0.091	15-12-2012
H_2O–5649	G133.563+01.019	02 23 52.2	+61 58 04	N	N	N	1	-	N	N	0.10	15-12-2012
H_2O–5650	G133.603+01.131	02 24 31.5	+62 03 31	Y	N	N	2	-	Y	N	0.079	15-12-2012
H_2O–5651	G133.616+00.111	02 21 39.8	+61 05 49	Y	N	N	2	-	Y	N	0.099	15-12-2012
H_2O–5652	G133.646+01.177	02 25 00.8	+62 05 11	Y	N	N	2	-	Y	N	0.21	18-10-2012
H_2O–5653	G133.663+01.185	02 25 10.0	+62 05 17	Y	N	N	2	-	Y	N	0.19	18-10-2012

Table 1 — *Continued*

ID	BGPS name (v1.0.1)	RA (J2000)	DEC (J2000)	WISE	HII	RMS	Phase	HCO^+ (S11)	HCO^+ (S13)	H_2O	rms Jy	date dd-mm-yyyy
(1)	(2)	(3)	(4)	(5)	(6)	(7)	(8)	(9)	(10)	(11)	(12)	(13)
H_2O–5654	G133.670+01.163	02 25 09.8	+62 03 53	Y	N	N	2	-	Y	N	0.18	18-10-2012
H_2O–5655	G133.694+01.215	02 25 30.8	+62 06 17	Y	N	Y	3	-	Y	N	0.25	18-10-2012
H_2O–5656	G133.715+01.217	02 25 40.8	+62 05 58	Y	Y	Y	3	-	Y	Y	6.4	18-10-2012
H_2O–5657	G133.717+00.659	02 24 01.6	+61 34 36	Y	N	N	2	-	N	N	0.21	18-10-2012
H_2O–5658	G133.718+01.113	02 25 23.7	+62 00 03	Y	N	N	2	-	N	N	0.21	18-10-2012
H_2O–5659	G133.727+00.621	02 23 59.6	+61 32 15	Y	N	N	2	-	N	N	0.23	18-10-2012
H_2O–5660	G133.729+01.283	02 25 59.5	+62 09 22	Y	N	N	2	-	Y	N	0.15	25-12-2013
H_2O–5661	G133.730+00.625	02 24 02.2	+61 32 24	Y	N	N	2	-	N	N	0.24	18-10-2012
H_2O–5662	G133.733+01.317	02 26 07.7	+62 11 12	N	N	N	1	-	Y	N	0.25	18-10-2012
H_2O–5663	G133.733+01.329	02 26 09.9	+62 11 52	Y	N	N	2	-	Y	N	0.24	18-10-2012
H_2O–5664	G133.735+01.085	02 25 26.3	+61 58 09	Y	N	N	2	-	Y	N	0.28	18-10-2012
H_2O–5665	G133.736+01.271	02 26 01.2	+62 08 32	Y	N	N	2	-	Y	N	0.33	18-10-2012
H_2O–5666	G133.739+01.335	02 26 13.9	+62 12 04	N	N	N	1	-	Y	N	0.26	18-10-2012
H_2O–5667	G133.748+01.059	02 25 28.3	+61 56 23	Y	N	N	2	-	Y	Y	0.30	18-10-2012
H_2O–5668	G133.748+01.197	02 25 53.4	+62 04 07	Y	N	Y	3	-	Y	Y	0.48	18-10-2012
H_2O–5669	G133.777+01.177	02 26 03.1	+62 02 24	Y	N	N	2	-	Y	N	0.33	18-10-2012
H_2O–5670	G133.778+01.201	02 26 08.5	+62 03 42	Y	N	N	2	-	Y	N	0.25	18-10-2012
H_2O–5671	G133.784+01.421	02 26 51.9	+62 15 54	Y	Y	N	3	-	N	N	0.096	15-12-2012
H_2O–5672	G133.790+01.107	02 25 57.0	+61 58 11	Y	N	N	2	-	Y	N	0.087	15-12-2012
H_2O–5673	G133.790+01.447	02 26 59.7	+62 17 13	Y	N	N	2	-	Y	N	0.10	15-12-2012
H_2O–5674	G133.801+01.225	02 26 23.4	+62 04 35	N	N	N	1	-	Y	N	0.091	15-12-2012
H_2O–5675	G133.811+01.267	02 26 35.9	+62 06 43	Y	N	N	2	-	Y	N	0.095	15-12-2012
H_2O–5676	G133.854+01.229	02 26 49.9	+62 03 38	Y	N	N	2	-	Y	N	0.095	15-12-2012
H_2O–5677	G133.865+01.057	02 26 23.2	+61 53 47	Y	N	N	2	-	Y	N	0.091	15-12-2012
H_2O–5678	G133.890+01.137	02 26 50.2	+61 57 43	Y	N	N	2	-	Y	N	0.081	15-12-2012
H_2O–5679	G133.902+01.355	02 27 36.3	+62 09 39	Y	N	N	2	-	Y	N	0.097	15-12-2012
H_2O–5680	G133.907+01.327	02 27 33.0	+62 07 59	N	N	N	1	-	N	N	0.11	15-12-2012
H_2O–5681	G133.913+01.409	02 27 51.1	+62 12 27	Y	N	N	2	-	N	N	0.096	15-12-2012
H_2O–5682	G133.914+01.395	02 27 49.5	+62 11 37	N	N	N	1	-	N	N	0.10	15-12-2012
H_2O–5683	G133.919+01.157	02 27 07.2	+61 58 13	Y	N	N	2	-	Y	N	0.10	15-12-2012
H_2O–5684	G133.949+01.063	02 27 04.2	+61 52 19	Y	Y	Y	3	-	Y	Y	1.8	15-12-2012
H_2O–5685	G133.961+01.121	02 27 20.5	+61 55 18	Y	Y	N	3	-	Y	N	0.11	15-12-2012
H_2O–5686	G133.965+00.851	02 26 33.1	+61 40 06	Y	N	N	2	-	N	N	0.10	15-12-2012
H_2O–5687	G133.968+00.877	02 26 39.7	+61 41 28	Y	N	N	2	-	N	N	0.10	15-12-2012
H_2O–5688	G133.985+00.427	02 25 26.4	+61 15 55	N	N	N	1	-	N	N	0.11	15-12-2012
H_2O–5689	G133.985+00.441	02 25 28.9	+61 16 42	Y	N	N	2	-	Y	N	0.11	15-12-2012
H_2O–5690	G133.997+00.519	02 25 48.4	+61 20 49	Y	N	N	2	-	Y	N	0.11	15-12-2012
H_2O–5691	G134.009+00.429	02 25 37.9	+61 15 30	N	N	N	1	-	Y	N	0.080	15-12-2012
H_2O–5692	G134.021+00.411	02 25 40.3	+61 14 15	Y	N	N	2	-	Y	N	0.090	15-12-2012
H_2O–5693	G134.025+00.413	02 25 42.6	+61 14 16	Y	N	N	2	-	Y	N	0.082	15-12-2012
H_2O–5694	G134.051+00.699	02 26 46.0	+61 29 44	Y	N	N	2	-	Y	N	0.090	15-12-2012
H_2O–5695	G134.074+00.709	02 26 59.0	+61 29 47	Y	N	N	2	-	Y	N	0.092	15-12-2012
H_2O–5696	G134.203+00.753	02 28 07.1	+61 29 27	Y	N	N	2	-	Y	N	0.096	15-12-2012
H_2O–5697	G134.211+00.621	02 27 46.7	+61 21 54	Y	N	N	2	-	N	N	0.081	15-12-2012
H_2O–5698	G134.211+00.729	02 28 06.4	+61 27 56	Y	N	N	2	-	Y	N	0.094	15-12-2012
H_2O–5699	G134.212+00.829	02 28 25.7	+61 33 29	Y	N	N	2	-	Y	N	0.080	15-12-2012
H_2O–5700	G134.218+00.787	02 28 20.8	+61 31 00	Y	N	N	2	-	Y	N	0.089	15-12-2012
H_2O–5701	G134.221+00.811	02 28 26.1	+61 32 18	Y	N	N	2	-	Y	N	0.081	15-12-2012
H_2O–5702	G134.236+00.639	02 28 02.1	+61 22 21	N	N	N	1	-	Y	N	0.077	15-12-2012
H_2O–5703	G134.241+00.751	02 28 24.5	+61 28 31	Y	Y	N	3	-	Y	N	0.082	15-12-2012
H_2O–5704	G134.265+01.147	02 29 49.4	+61 50 04	Y	N	N	2	-	Y	N	0.083	15-12-2012
H_2O–5705	G134.281+00.855	02 29 02.4	+61 33 26	Y	Y	Y	3	-	Y	Y	0.089	15-12-2012
H_2O–5706	G134.817+01.355	02 34 49.2	+61 49 03	N	N	N	1	-	Y	N	0.090	15-12-2012
H_2O–5707	G134.830+01.317	02 34 48.2	+61 46 37	Y	N	N	2	-	Y	N	0.090	15-12-2012
H_2O–5708	G134.896+01.545	02 36 04.4	+61 57 41	Y	N	N	2	-	Y	N	0.10	15-12-2012
H_2O–5709	G135.637+02.431	02 44 58.1	+62 28 08	Y	N	N	2	-	N	N	0.080	15-12-2012
H_2O–5710	G135.891−00.461	02 37 05.7	+59 43 33	Y	N	N	2	-	Y	Y	0.095	15-12-2012
H_2O–5711	G136.223+01.082	02 44 38.5	+60 59 52	Y	N	N	2	Y	Y	N	0.099	15-12-2012
H_2O–5712	G136.384+02.268	02 50 09.1	+61 59 53	Y	Y	Y	3	Y	Y	Y	0.095	15-12-2012
H_2O–5713	G136.512+01.196	02 47 11.4	+60 58 41	N	N	N	1	-	N	N	0.098	15-12-2012
H_2O–5714	G136.533+01.232	02 47 28.9	+61 00 04	N	N	N	1	Y	Y	N	0.096	15-12-2012
H_2O–5715	G136.539+01.238	02 47 32.9	+61 00 14	N	N	N	1	Y	Y	N	0.10	15-12-2012
H_2O–5716	G136.671+01.212	02 48 26.2	+60 55 24	Y	N	N	2	Y	Y	N	0.10	15-12-2012
H_2O–5717	G136.716+01.332	02 49 11.6	+61 00 43	Y	N	N	2	N	N	N	0.096	15-12-2012
H_2O–5718	G136.719+00.782	02 47 16.1	+60 30 54	Y	Y	N	3	Y	Y	N	0.13	15-12-2012
H_2O–5719	G136.825+01.140	02 49 19.0	+60 47 29	N	N	N	1	N	N	N	0.13	15-12-2012
H_2O–5720	G136.825+01.130	02 49 16.8	+60 46 57	Y	N	N	2	N	N	N	0.14	15-12-2012
H_2O–5721	G136.849+01.150	02 49 31.7	+60 47 23	Y	N	N	2	Y	Y	Y	0.12	15-12-2012

Table 1 — *Continued*

ID	BGPS name (v1.0.1)	RA (J2000)	DEC (J2000)	WISE	HII	RMS	Phase	HCO^+ (S11)	HCO^+ (S13)	H_2O	rms Jy	date dd-mm-yyyy
(1)	(2)	(3)	(4)	(5)	(6)	(7)	(8)	(9)	(10)	(11)	(12)	(13)
H_2O–5722	G136.891+01.100	02 49 39.5	+60 43 35	N	N	N	1	Y	Y	N	0.12	15-12-2012
H_2O–5723	G136.914+01.092	02 49 47.5	+60 42 34	Y	Y	N	3	-	Y	N	0.13	15-12-2012
H_2O–5724	G136.945+01.092	02 50 01.6	+60 41 44	Y	N	N	2	-	Y	Y	0.12	15-12-2012
H_2O–5725	G136.979+01.118	02 50 22.2	+60 42 14	Y	N	N	2	-	Y	N	0.15	15-12-2012
H_2O–5726	G137.067+03.004	02 58 13.3	+62 20 38	N	N	N	1	-	Y	Y	0.19	15-12-2012
H_2O–5727	G137.481+00.638	02 52 16.9	+60 03 02	Y	N	N	2	-	Y	N	0.17	16-12-2012
H_2O–5728	G137.506+01.394	02 55 13.6	+60 42 50	N	N	N	1	-	Y	N	0.15	16-12-2012
H_2O–5729	G137.538+01.276	02 55 01.0	+60 35 40	Y	N	N	2	-	Y	N	0.20	16-12-2012
H_2O–5730	G137.586+01.312	02 55 29.9	+60 36 16	Y	N	N	2	-	Y	N	0.19	16-12-2012
H_2O–5731	G137.617+01.350	02 55 52.4	+60 37 24	N	N	N	1	-	Y	N	0.17	16-12-2012
H_2O–5732	G137.634+01.508	02 56 35.1	+60 45 23	Y	N	N	2	-	N	N	0.21	16-12-2012
H_2O–5733	G137.665+01.526	02 56 53.1	+60 45 27	Y	N	N	2	-	N	N	0.23	16-12-2012
H_2O–5734	G137.705+01.490	02 57 02.3	+60 42 25	Y	N	N	2	-	Y	N	0.12	21-01-2013
H_2O–5735	G137.707+01.442	02 56 52.3	+60 39 49	Y	N	N	2	-	N	N	0.11	21-01-2013
H_2O–5736	G137.713+01.442	02 56 54.9	+60 39 39	Y	N	N	2	-	N	N	0.12	21-01-2013
H_2O–5737	G137.713+01.472	02 57 01.7	+60 41 15	Y	N	N	2	-	Y	N	0.13	21-01-2013
H_2O–5738	G137.744+01.492	02 57 19.3	+60 41 28	Y	N	N	2	-	Y	N	0.13	21-01-2013
H_2O–5739	G137.770+01.450	02 57 21.0	+60 38 31	N	N	N	1	-	Y	N	0.14	21-01-2013
H_2O–5740	G137.780+01.458	02 57 27.1	+60 38 39	Y	N	N	2	-	Y	N	0.14	21-01-2013
H_2O–5741	G138.144+01.682	03 00 56.1	+60 40 14	Y	N	N	2	-	Y	N	0.13	21-01-2013
H_2O–5742	G138.295+01.556	03 01 31.9	+60 29 13	Y	Y	Y	3	-	Y	N	0.079	23-01-2013
H_2O–5743	G138.466+01.632	03 03 02.3	+60 28 19	Y	N	N	2	-	Y	N	0.076	23-01-2013
H_2O–5744	G138.469+01.584	03 02 52.7	+60 25 41	Y	N	N	2	-	N	N	0.076	23-01-2013
H_2O–5745	G138.503+01.646	03 03 21.8	+60 27 57	Y	N	N	2	-	Y	Y	0.093	23-01-2013
H_2O–5746	G188.792+01.027	06 09 05.9	+21 50 39	Y	Y	N	3	-	Y	Y	0.40	23-01-2013
H_2O–5747	G188.948+00.883	06 08 52.9	+21 38 16	Y	Y	Y	3	-	Y	Y	0.057	23-01-2013
H_2O–5748	G188.975+00.911	06 09 02.7	+21 37 37	Y	N	N	2	-	Y	N	0.047	23-01-2013
H_2O–5749	G188.991+00.859	06 08 52.9	+21 35 16	Y	N	N	2	-	Y	N	0.052	23-01-2013
H_2O–5750	G189.015+00.823	06 08 47.8	+21 32 58	Y	N	N	2	-	Y	Y	0.047	23-01-2013
H_2O–5751	G189.030+00.781	06 08 40.1	+21 31 01	Y	Y	Y	3	-	Y	N	0.043	23-01-2013
H_2O–5752	G189.032+00.793	06 08 43.1	+21 31 15	Y	N	Y	3	-	Y	N	0.036	23-01-2013
H_2O–5753	G189.116+00.643	06 08 19.7	+21 22 29	N	N	N	1	-	N	N	0.055	23-01-2013
H_2O–5754	G189.231+00.893	06 09 30.6	+21 23 39	Y	Y	N	3	-	Y	N	0.053	23-01-2013
H_2O–5755	G189.646+00.131	06 07 30.9	+20 39 46	N	N	N	1	-	N	N	0.051	23-01-2013
H_2O–5756	G189.659+00.185	06 07 44.7	+20 40 36	Y	N	N	2	-	N	N	0.054	23-01-2013
H_2O–5757	G189.682+00.185	06 07 47.5	+20 39 27	Y	N	N	2	-	Y	N	0.086	22-01-2013
H_2O–5758	G189.713+00.335	06 08 25.1	+20 42 09	N	N	N	1	-	Y	N	0.085	22-01-2013
H_2O–5759	G189.744+00.335	06 08 28.8	+20 40 34	Y	N	N	2	-	Y	N	0.070	22-01-2013
H_2O–5760	G189.776+00.343	06 08 34.6	+20 39 07	Y	N	N	2	-	Y	Y	0.072	22-01-2013
H_2O–5761	G189.782+00.265	06 08 17.8	+20 36 32	Y	N	N	2	-	Y	N	0.069	22-01-2013
H_2O–5762	G189.782+00.323	06 08 30.8	+20 38 13	Y	N	N	2	-	Y	N	0.18	11-09-2012
H_2O–5763	G189.783+00.433	06 08 55.8	+20 41 20	Y	N	N	2	-	Y	N	0.072	22-01-2013
H_2O–5764	G189.783+00.465	06 09 03.0	+20 42 15	Y	N	N	2	-	Y	N	0.065	22-01-2013
H_2O–5765	G189.788+00.281	06 08 22.2	+20 36 41	N	N	N	1	-	Y	N	0.066	22-01-2013
H_2O–5766	G189.789+00.291	06 08 24.6	+20 36 52	N	N	N	1	-	Y	N	0.080	22-01-2013
H_2O–5767	G189.804+00.355	06 08 40.8	+20 38 00	Y	N	N	2	-	Y	N	0.065	22-01-2013
H_2O–5768	G189.810+00.369	06 08 44.6	+20 38 06	Y	N	N	2	-	Y	N	0.073	22-01-2013
H_2O–5769	G189.831+00.343	06 08 41.5	+20 36 11	Y	N	N	2	-	Y	N	0.069	22-01-2013
H_2O–5770	G189.834+00.317	06 08 36.0	+20 35 19	Y	N	N	2	-	Y	N	0.064	22-01-2013
H_2O–5771	G189.836+00.303	06 08 33.1	+20 34 49	Y	N	N	2	-	Y	N	0.072	22-01-2013
H_2O–5772	G189.864+00.499	06 09 20.5	+20 39 02	Y	Y	Y	3	-	Y	N	0.071	22-01-2013
H_2O–5773	G189.879+00.319	06 08 42.1	+20 32 58	Y	N	N	2	-	Y	N	0.082	22-01-2013
H_2O–5774	G189.885+00.319	06 08 42.9	+20 32 39	Y	N	N	2	-	Y	N	0.087	22-01-2013
H_2O–5775	G189.888+00.303	06 08 39.6	+20 32 05	Y	N	N	2	-	Y	N	0.072	22-01-2013
H_2O–5776	G189.921+00.331	06 08 50.0	+20 31 06	Y	N	N	2	-	Y	N	0.074	22-01-2013
H_2O–5777	G189.950+00.231	06 08 31.1	+20 26 44	Y	N	N	2	-	Y	N	0.080	22-01-2013
H_2O–5778	G189.951+00.331	06 08 53.8	+20 29 32	Y	N	N	2	-	Y	N	0.089	22-01-2013
H_2O–5779	G189.990+00.353	06 09 03.4	+20 28 11	Y	N	N	2	-	Y	N	0.078	22-01-2013
H_2O–5780	G190.006+00.361	06 09 07.2	+20 27 34	Y	N	N	2	-	Y	N	0.085	22-01-2013
H_2O–5781	G190.044+00.543	06 09 52.7	+20 30 52	Y	Y	N	3	-	Y	N	0.10	22-01-2013
H_2O–5782	G190.054+00.533	06 09 51.7	+20 30 03	Y	Y	N	3	-	Y	Y	0.098	22-01-2013
H_2O–5783	G190.063+00.679	06 10 25.7	+20 33 45	Y	N	N	2	-	Y	N	0.10	22-01-2013
H_2O–5784	G190.171+00.733	06 10 51.2	+20 29 38	Y	N	N	2	-	Y	N	0.10	22-01-2013
H_2O–5785	G190.192+00.719	06 10 50.5	+20 28 11	N	N	N	1	-	Y	N	0.11	22-01-2013
H_2O–5786	G190.240+00.911	06 11 39.5	+20 31 12	N	N	N	1	-	Y	N	0.15	22-01-2013
H_2O–5787	G192.581−00.043	06 12 52.9	+18 00 29	Y	Y	Y	3	-	Y	N	0.15	18-08-2013
H_2O–5788	G192.596−00.051	06 12 52.8	+17 59 30	Y	Y	Y	3	-	Y	Y	0.39	22-01-2013
H_2O–5789	G192.602−00.143	06 12 33.1	+17 56 33	Y	N	N	2	-	Y	N	0.54	22-01-2013

Table 1 — *Continued*

ID	BGPS name (v1.0.1)	RA (J2000)	DEC (J2000)	WISE	HII	RMS	Phase	HCO^+ (S11)	HCO^+ (S13)	H_2O	rms Jy	date dd-mm-yyyy
(1)	(2)	(3)	(4)	(5)	(6)	(7)	(8)	(9)	(10)	(11)	(12)	(13)
H_2O–5790	G192.629−00.123	06 12 41.0	+17 55 39	Y	N	N	2	-	Y	N	0.51	22-01-2013
H_2O–5791	G192.629−00.157	06 12 33.5	+17 54 40	Y	N	N	2	-	Y	N	0.71	22-01-2013
H_2O–5792	G192.644+00.003	06 13 10.5	+17 58 32	Y	N	N	2	-	Y	N	0.86	22-01-2013
H_2O–5793	G192.662−00.083	06 12 53.7	+17 55 07	Y	N	N	2	-	Y	N	0.075	23-01-2013
H_2O–5794	G192.719+00.043	06 13 28.6	+17 55 41	Y	Y	N	3	-	Y	N	0.073	23-01-2013
H_2O–5795	G192.764+00.101	06 13 46.8	+17 55 02	Y	N	N	2	-	Y	N	0.081	23-01-2013
H_2O–5796	G192.816+00.127	06 13 58.8	+17 53 03	Y	N	N	2	-	Y	N	0.075	23-01-2013
H_2O–5797	G192.968+00.093	06 14 09.6	+17 44 03	N	N	N	1	-	Y	N	0.069	23-01-2013
H_2O–5798	G192.981+00.149	06 14 23.7	+17 44 56	Y	Y	N	3	-	Y	N	0.079	23-01-2013
H_2O–5799	G192.985+00.177	06 14 30.3	+17 45 31	Y	N	N	2	-	Y	N	0.080	23-01-2013
H_2O–5800	G193.006+00.115	06 14 19.0	+17 42 42	Y	N	N	2	-	Y	N	0.077	23-01-2013

In our survey, single point observation mode was used to search for H_2O masers. The limited time led us to not perform OTF observations towards detected H_2O masers to derive the maser positions. We used data from the BeSSeL[5] survey observed using the VLA to inspect the association between BGPS sources and the H_2O masers we detected. We derived the precise position of H_2O masers by comparing the positions and velocities of H_2O masers, in which 2 arcmin ($\sim$ HPBW) was used for matching H_2O masers. There were five H_2O masers ($H_2O-5562$ G099.981+04.168, $H_2O-5684$ G133.949+01.063, $H_2O-5746$ G188.792+01.027, $H_2O-5747$ G188.948+00.883 and $H_2O-5760$ G189.776+00.343) which had been previously observed using the VLA. We found that all of these five masers were within the elliptical region encompassed by the BGPS source. Hence, these five masers were associated with the BGPS sources, assuming that they are not chance alignments along the line of sight. Considering the comparison above, most of the H_2O masers we detected are associated with the BGPS sources. However, there may be some cases where the masers that we detected were not associated the BGPS sources that we observed due to the large beam size of Nanshan. Further OTF or high resolution observations are also needed to confirm the location of the new detections.

Comparing with previous works, we found there were 10 sources associated with H_2O masers in which no H_2O masers were detected in our observation. Four of ten ($H_2O-5559$ G098.856+02.932, $H_2O-5671$ G133.784+01.421, $H_2O-5742$ G138.295+01.556, and $H_2O-5798$ G192.981+00.149) were observed by Valdettaro et al. (2001), but negative results were obtained. In our observation, the rms was about a tenth of or lower than that in Valdettaro et al. (2001). Further observations towards these sources are needed to confirm whether H_2O maser emission is associated with these regions. In four of the ten sources ($H_2O-5592$ G110.795+00.382, $H_2O-5604$ G111.284−00.664, $H_2O-5634$ G111.876+00.818 and $H_2O-5751$ G189.030+00.781), the flux densities of H_2O masers detected in previous works were above the rms in our observation. The masers should be detected in our observation, if we assume that the flux density of the H_2O maser is invariable. But the negative results suggest that the missed H_2O masers could be caused by variation of H_2O masers. In one of the ten sources ($H_2O-5655$ G133.694+01.215), the flux density of the H_2O maser in the previous work was about ten times as intense as the rms in our observation. The H_2O maser was not distinguished from the shadow of the nearby intense H_2O maser (H_2O–5655 G133.715+01.217 W3 IRS 5). Hence, the large beam size of Nanshan had some influence on our detection result. In one of ten sources ($H_2O-5576$ G110.113+00.050), the flux density of the H_2O maser was lower than 3$\times$rms in our observation. Therefore, we did not detect the maser. Hence, the sensitivity of the observation also influenced the results of our observation. Compared with the results obtained in previous works, we could estimate that the missed H_2O masers were mainly caused by variation of H_2O masers. The large beam size of the telescope and the sensitivity of the observation also had some influence on the result of observation.

4 INDIVIDUAL SOURCES

Most of the sources we detected had previously been observed. The H_2O masers in previous works were matched with the detection in our observation, if the masers are within 135″ (HPBW of the Nanshan telescope) from BGPS sources and have a similar velocity range. We perform a comparison between our detection and previous observations. The variation of H_2O masers in peak flux density, peak velocity and velocity range will be analyzed in the following part.

$H_2O-5551$ G085.412+00.002: Urquhart et al. (2011) detected this H_2O maser with a velocity range from -39.6 km s^{-1} to -12.9 km s^{-1}. The peak velocity was located at -32.5 km s^{-1} with peak flux density of 69.2 Jy. In our detection, the maser has a narrower velocity range from -39.6 km s^{-1} to -27.4 km s^{-1}. The feature located at -32.5 km s^{-1} has disappeared, and the most intense feature instead appears at -34.1 km s^{-1}. The peak flux density decreases to 24 Jy.

$H_2O-5556$ G088.096+00.413: Sunada et al. (2007) detected this H_2O maser whose velocity ranges from

[5] *http://bessel.vlbi-astrometry.org/home*

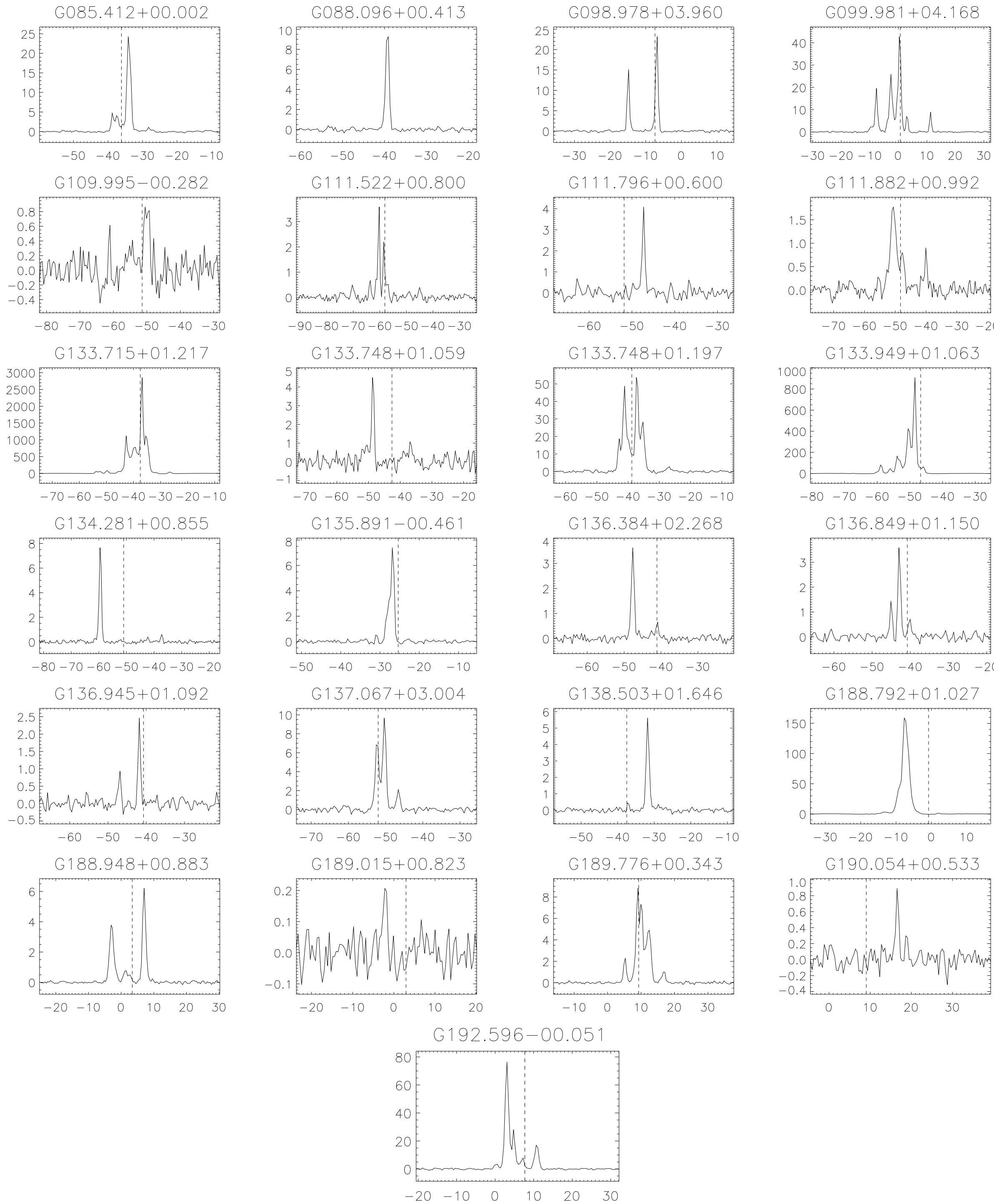

Fig. 1 Spectra of 22 GHz water masers. The dashed line represents the systematic velocity.

-47.0 km s^{-1} to -38.5 km s^{-1}. The peak feature was located at -43.9 km s^{-1} with flux density of 6.99 Jy. We detected this maser in our observation. We only detected one feature located at -39.1 km s^{-1} in the spectrum, and the velocity range was from -40.8 km s^{-1} to -38.2 km s^{-1}. The peak flux density has increased to be 9.3 Jy in our observations.

H_2O−5560 G098.978+03.960: This H_2O maser is a new detection which shows a double peak in the spectrum. The peak feature is located at -6.8 km s^{-1} and has a flux density of 23 Jy.

H_2O−5562 G099.981+04.168: This source is also known as WB110. This H_2O maser was detected by Bae et al. (2011). The velocity range was from -20.96 km s^{-1} to 3.27 km s^{-1}, and the most intense feature was located

Table 2 Parameters of H_2O Masers

ID (1)	BGPS name (v1.0.1) (2)	RA (J2000) (3)	DEC (J2000) (4)	$F_{\rm peak}$ (Jy) (5)	$V_{\rm peak}$ (km s^{-1}) (6)	$V_{\rm range}$ (km s^{-1}) (7)	S_ν (Jy km s^{-1}) (8)	rms (Jy) (9)	Ref (10)
$H_2O-5551$	G085.412+00.002	20:54:14	+44:54:07	24	−34.1	−39.6, −27.4	45	0.16	[4]
$H_2O-5556$	G088.096+00.413	21:02:33	+47:12:09	9.3	−39.1	−40.8, −38.2	10	0.14	[2]
$H_2O-5560$	G098.978+03.960	21:36:08	+57:26:48	23	−6.8	−15.6, −5.9	32	0.17	new
$H_2O-5562$	G099.981+04.168 (WB110)	21:40:42	+58:16:01	43	0.4	−10.6, 12.2	1.3×10^2	0.19	[3]
$H_2O-5564$	G109.995−00.282	23:05:23	+59:53:58	0.86	−50.5	−61.5, −48.8	2.0	0.17	[1]
$H_2O-5612$	G111.522+00.800	23:13:32	+61:29:03	3.6	−60.2	−71.2, −44.6	7.2	0.094	[4]
$H_2O-5632$	G111.796+00.600	23:16:16	+61:23:51	4.1	−47.3	−48.1, −46.4	3.1	0.23	new
$H_2O-5635$	G111.882+00.992	23:15:46	+61:47:39	1.8	−50.6	−53.1, −39.2	6.4	0.11	[2]
$H_2O-5656$	G133.715+01.217 (W3 IRS 5)	02:25:40	+62:05:58	2.9×10^3	−36.8	−54.5, −25.8	9.3×10^3	6.4	[4]
$H_2O-5667$	G133.748+01.059	02:25:28	+61:56:23	4.5	−48.7	−49.6, −36.1	5.5	0.30	new
$H_2O-5668$	G133.748+01.197 (W3 3)	02 25 53	+62 04 07	54	−37.3	−44.1, −26.4	2.2×10^2	0.48	[1]
$H_2O-5684$	G133.949+01.063 (W3 OH)	02:27:04	+61:52:19	9.1×10^2	−48.4	−60.7, −44.6	2.1×10^3	1.8	[2]
$H_2O-5705$	G134.281+00.855	02:29:02	+61:33:26	7.7	−59.6	−61.7, −36.4	9.2	0.089	[1]
$H_2O-5710$	G135.891−00.461	02:37:05	+59:43:32	7.4	−26.9	−31.5, −25.6	11	0.095	[1]
$H_2O-5712$	G136.384+02.268	02:50:09	+61:59:53	3.6	−47.6	−48.9, −40.5	4.7	0.095	[4]
$H_2O-5721$	G136.849+01.150	02:49:31	+60:47:23	3.6	−43.0	−45.5, −39.6	4.8	0.12	[1]
$H_2O-5724$	G136.945+01.092	02:50:01	+60:41:44	2.5	−41.8	−47.7, −41.0	2.6	0.12	new
$H_2O-5726$	G137.067+03.004	02:58:13	+62:20:38	9.7	−50.4	−53.8, −45.7	23	0.19	[2]
$H_2O-5745$	G138.503+01.646 (S201)	03:03:21	+60:27:57	5.6	−31.8	−37.7, −28.5	6.3	0.09	[2]
$H_2O-5746$	G188.792+01.027 (Gem 1)	06:09:06	+21:50:39	1.6×10^2	−7.7	−14.4, −3.0	4.1×10^2	0.40	[2]
$H_2O-5747$	G188.948+00.883	06:08:52	+21:38:16	6.2	7.0	−4.8, 10.0	16	0.057	[2]
$H_2O-5750$	G189.015+00.823	06:08:47	+21:32:58	0.21	−2.2	−2.6, −1.4	0.24	0.047	new
$H_2O-5760$	G189.776+00.343 (S252 A)	06:08:35	+20:39:08	8.8	9.1	4.0, 17.6	31	0.072	[2]
$H_2O-5782$	G190.054+00.533	06:09:51	+20:30:03	0.89	16.5	15.7, 19.1	1.0	0.098	[1]
$H_2O-5788$	G192.596−00.051 (S255/7)	06:12:52	+17:59:31	76	3.1	−0.7, 11.9	1.5×10^2	0.39	[2]

Notes: Col. (1) gives the indices of BGPS sources in our survey. Col. (2) shows the name of BGPS source in catalog v1.0.1, followed by well known names. Cols. (3) and (4) give the coordinates of peak position of BGPS source in J2000 where we search for an H_2O maser. The peak flux density, peak velocity, velocity range and integrated flux density of the H_2O maser are listed in Cols. (5) to (8). The rms in each spectrum is given in Col. (9). The references are listed in Col. (10). These references correspond to: [1] Valdettaro et al. (2001), [2] Sunada et al. (2007), [3] Bae et al. (2011), [4] Urquhart et al. (2011).

at −10.01 km s^{-1} with a flux density of 27.08 Jy. In our detections, the velocity range was from –10.6 km s^{-1} to 12.2 km s^{-1}. The feature located at 11.2 km s^{-1} was a new detection. The peak velocity was at 0.4 km s^{-1}, and the peak flux density increased to 43 Jy.

$H_2O-5564$ G109.995−00.282: This H_2O maser was discovered by Wouterloot & Walmsley (1986). Valdettaro et al. (2001) performed a re-observation towards this source. However, a negative result was obtained with an rms of 2.1 Jy between −136.3 km s^{-1} and 32.3 km s^{-1}. This may be due to the high rms. We detected this maser in our sensitive observation (rms 0.17 Jy). The maser has a velocity range from −61.5 km s^{-1} to −48.8 km s^{-1}. The peak feature has flux density of 0.86 Jy located at −50.5 km s^{-1}.

$H_2O-5612$ G111.522+00.800: Urquhart et al. (2011) detected this H_2O maser to have a velocity range from −85.1 km s^{-1} to −65.0 km s^{-1}. The peak flux density was 102.4 Jy which was located at −71.2 km s^{-1}. In our observation, we also detected this maser. The velocity range varied from −71.2 km s^{-1} to −44.6 km s^{-1}. The most intense feature at −71.2 km s^{-1} in Urquhart et al. (2011) was also seen in our observation, but the flux density was very weak (only a few tenths of a Jy). This maser had peak flux density of 3.6 Jy at −60.2 km s^{-1}. The peak flux density of this maser has decreased over a three year period to only a few percent of that observed by Urquhart et al. (2011).

$H_2O-5632$ G111.796+00.600: This is a new detection. Only a single feature appears in the spectrum. The peak flux density was 4.1 Jy at −47.3 km s^{-1}. The velocity range was from −48.1 km s^{-1} to −46.4 km s^{-1}.

$H_2O-5635$ G111.882+00.992: Sunada et al. (2007) detected this maser whose peak flux density was 7.45 Jy at −44.01 km s^{-1}, and the velocity range was from −58.5 km s^{-1} to −40.5 km s^{-1}. In our observation, the velocity range was from −53.1 km s^{-1} to −39.2 km s^{-1}. The most intense feature had vanished in our observation. Instead the peak flux density was 1.8 Jy at −50.6 km s^{-1}.

$H_2O-5656$ G133.715+01.217: This source is the well-known source W3 IRS 5. Urquhart et al. (2011) detected this H_2O maser. The velocity range of the maser was from −80.9 km s^{-1} to 5.5 km s^{-1}, and the most intense feature had flux density of 1.5×10^4 Jy at −39.5 km s^{-1}. This is the most intense maser in our observation. The velocity range was from −54.5 km s^{-1} to −25.8 km s^{-1}, which is narrower than that in Urquhart et al. (2011). The most intense feature at –39.5 km s^{-1} in Urquhart et al. (2011) has become the fourth most intense feature. The most intense feature in our observation had a flux density of 2.9×10^3 Jy at –36.8 km s^{-1}. This maser had decreased by more than 10^4 Jy. Urquhart et al. (2011) may have observed this source during an outburst in the maser activity.

$H_2O-5667$ G133.748+01.059: This is a newly detected H_2O maser. The velocity range was from

-49.6 km s^{-1} to -36.1 km s^{-1}. The peak flux density was 4.5 Jy at -48.7 km s^{-1}.

$H_2O-5668$ G133.748+01.197: The source is also known as W3 3. Valdettaro et al. (2001) detected this H_2O maser with a velocity range from -49.4 km s^{-1} to -30.3 km s^{-1}. The peak velocity was at -39.3 km s^{-1} with a flux density of 69.65 Jy. In our observations, a similar velocity range was detected from -44.1 km s^{-1} to –26.4 km s^{-1}. The peak velocity was located at -37.3 km s^{-1}, and the peak flux density was 54 Jy in our observations.

$H_2O-5684$ G133.949+01.063: Sunada et al. (2007) detected this H_2O maser having a wide velocity range from -111.5 km s^{-1} to 6.0 km s^{-1}. The most intense feature was located at -46.8 km s^{-1} with a flux density of 659.34 Jy. We detected this maser as showing a much narrower velocity range from -60.7 km s^{-1} to -44.6 km s^{-1}. The weak features were not detected in the spectrum which may be caused by high rms of 1.9 Jy. The peak flux density was 9.1×10^2 Jy at -48.4 km s^{-1}. The most intense feature detected by Sunada et al. (2007) was not detected in our observations.

$H_2O-5705$ G134.281+00.855: Xiang & Turner (1995) discovered this maser, and Valdettaro et al. (2001) performed re-observation toward this source. However, a negative result was obtained in their observation with the velocity coverage from -110.0 km s^{-1} to 110 km s^{-1}. The spectrum of this source in our observation showed an intense feature accompanying a few weak features. The most intense feature was located at -59.6 km s^{-1} with flux density of 7.7 Jy. The velocity range was from -62.7 km s^{-1} to -36.4 km s^{-1}.

$H_2O-5710$ G135.891−00.461: Observations by Valdettaro et al. (2001) did not detect any H_2O maser emission in this source in the velocity range from -72.1 km s^{-1} to 12.1 km s^{-1}. This maser was detected in our observation. The maser had a velocity range from -31.5 km s^{-1} to -25.6 km s^{-1}. The peak flux density was 7.4 Jy at -26.9 km s^{-1}.

$H_2O-5712$ G136.384+02.268: Urquhart et al. (2011) detected this maser showing a velocity range from -48.6 km s^{-1} to -37.6 km s^{-1}. The peak flux density was 30.0 Jy at -45.8 km s^{-1}. We detected this maser in our observation. But the most intense feature detected in Urquhart et al. (2011) had vanished, and instead the peak flux density in our observation was 3.6 Jy at -47.6 km s^{-1}, which was just a tenth of that in Urquhart et al. (2011).

$H_2O-5721$ G136.849+01.150: Han et al. (1998) discovered this H_2O maser. A re-observation was performed by Valdettaro et al. (2001) with velocity coverage from -130.0 km s^{-1} to 86.0 km s^{-1}, but a negative result was obtained. In our observation, this maser had velocity range from -45.5 km s^{-1} to -39.6 km s^{-1}. The peak feature was located at -43.0 km s^{-1} with a flux density of 3.6 Jy.

$H_2O-5724$ G136.945+01.092: This is a newly detected H_2O maser. Two peaks are observed in the spectrum. The velocity range was from -47.7 km s^{-1} to -41.0 km s^{-1}. The peak flux density was 2.5 Jy at -41.8 km s^{-1}.

$H_2O-5726$ G137.067+03.004: Sunada et al. (2007) detected this H_2O maser showing a velocity range from -59.0 km s^{-1} to -38.0 km s^{-1}, and the peak flux density was 10.99 Jy at –50.8 km s^{-1}. In our observation, the maser showed a narrower velocity range from -53.8 km s^{-1} to -45.7 km s^{-1}. The peak flux density was 9.7 Jy at -50.4 km s^{-1} in our observation. Because the velocity resolution was 0.44 km s^{-1} in our spectrum, the peak feature that we detected was also the one detected in Sunada et al. (2007).

$H_2O-5745$ G138.503+01.646: This source is also known as S201. Sunada et al. (2007) detected this H_2O maser. The maser had a velocity range from -37.5 km s^{-1} to -30.0 km s^{-1}, and the peak flux density was 0.97 Jy at -35.2 km s^{-1}. We detected this maser with velocity range from -37.7 km s^{-1} to -28.5 km s^{-1} which was very similar to the previous observation. The peak flux density was 5.6 Jy at -31.8 km s^{-1}, so the maser has increased in intensity by a factor of approximately five.

$H_2O-5746$ G188.792+01.027: This source is known as Gem 1. Sunada et al. (2007) detected this H_2O maser with velocity range from -25.0 km s^{-1} to 5.5 km s^{-1}. The peak feature was located at -7.7 km s^{-1} with flux density of 265.33 Jy. We detected this maser as well. The maser showed a velocity range from -14.4 km s^{-1} to -3.0 km s^{-1}. We detected the same peak feature at -7.7 km s^{-1} with a flux density of 1.6×10^2 Jy. The peak flux density has decreased by 100 Jy.

$H_2O-5747$ G188.948+00.883: Sunada et al. (2007) detected this H_2O maser showing a velocity range from -9.0 km s^{-1} to 7.5 km s^{-1}, and a peak flux density of 20.09 Jy at 2.5 km s^{-1}. We detected this maser which had a velocity range from -4.8 km s^{-1} to 10.0 km s^{-1}. The peak velocity was at 7.0 km s^{-1}, and the peak flux density was 6.2 Jy.

$H_2O-5750$ G189.015+00.823: This H_2O maser is a new detection. The maser had a velocity range from -2.6 km s^{-1} to -1.4 km s^{-1}. Only one feature is detected in the spectrum, and it is relatively weak with a peak flux density of 0.21 Jy (about four times the rms noise). The peak velocity was located at -2.2 km s^{-1}.

$H_2O-5760$ G189.776+00.343: This source is also known as S252 A. Sunada et al. (2007) performed multi-epoch observations towards this source. The peak flux density varied from 3.20 Jy to 0.64 Jy in a year. The last observation gave the velocity range of the maser from 12.0 km s^{-1} to 14.5 km s^{-1} and the peak flux density of 0.64 Jy at 13.3 km s^{-1}. In our observations, the velocity range was from 4.0 km s^{-1} to 17.6 km s^{-1}. The most intense feature detected in Sunada et al. (2007) had vanished, and instead the peak feature was at 9.1 km s^{-1}. The peak flux density is 8.8 Jy which is an increase by a factor of 10 from the last observation by Sunada et al. (2007).

$H_2O-5782$ G190.054+00.533: Han et al. (1998) discovered this H_2O maser. Valdettaro et al. (2001) performed additional observations of this source, but did not detect any emission in the velocity range from -151.0 km s^{-1} to 63.0 km s^{-1} with an rms of 0.72 Jy. In our observation, the maser had velocity range from 15.7 km s^{-1} to 19.1 km s^{-1}. The most intense feature was located at 16.5 km s^{-1} with a flux density of 0.89 Jy.

H_2O−5788 G192.596−00.051: This source is known as S255/7. Sunada et al. (2007) detected this H_2O maser in two epochs of observations. The peak flux density varied from 27.46 Jy to 88.12 Jy in half a year. The velocity range was from –9.0 km s^{-1} to 14.5 km s^{-1}, and peak flux density was 88.12 Jy at 2.3 km s^{-1} in the last observation by Sunada et al. (2007). We detected this maser showing a velocity range from -0.7 km s^{-1} to 11.9 km s^{-1}. The peak velocity was located at 3.1 km s^{-1}. The peak flux density in our observations was 76 Jy, which was similar to the observation result of Sunada et al. (2007).

5 DISCUSSION

5.1 The Influence Radius of a Strong H_2O Maser

Due to the large beam size of the telescope, we find that H_2O maser spectra detected at nine different positions show nearly the same line profile but with different flux density (see Fig. 2). Four features of all of the spectra appear at the same velocity which strongly suggests that these nine spectra come from one H_2O maser. It is reasonable to believe that the strongest one is the true detection and the others are fake detections. Valdettaro et al. (2001) demonstrated that the emission of the strong maser can be seen in the side lobes up to an angular distance of 30 HPBWs from a large region mapped toward Orion KL. If our interpretation of your meaning is not correct, please explain your meaning more clearly. If we assume that the strongest H_2O maser G133.715+01.217 is a true detection, then it was also detected at eight other nearby sources (see Fig. 2). We may obtain the influence radius for a given intensity flux density of an H_2O maser by plotting the peak flux density as a function of angular distance. This could help us to eliminate fake detections from real ones.

We plot the peak flux density as a function of angular distance in Figure 3. The flux density is in log-scale and the angular distance is in the unit of HPBW. It clearly shows that the peak flux density decreases as an exponential function of the angular distance. We perform the linear fitting between the peak flux density in log-scale and angular distance in the unit of HPBW. The best fitting linear line is plotted as a solid line. The dotted line represents the average rms (0.17 Jy) in our observation. We can see that an H_2O maser with flux density of 3×10^3 Jy can be seen as far as five HPBWs away from its true position. We assume that the correlation between detected flux density and angular distance is the same as that shown in Figure 3. The best fitting formula for the Nanshan 25 m radio telescope is $F = F_0 \times 10^{-0.8d}$, where F_0 is the flux density of the H_2O maser, d is the angular distance to the H_2O maser in the unit of HPBW, and F is the detected flux density at an angular distance of d. If the rms is given and a feature with S/N above 3 is considered as a maser detection, then the influence radius is given by $r = \frac{1}{0.8}\log(\frac{F_0}{3\mathrm{rms}})$.

For the most intense H_2O maser in W49N with flux density of $\sim 10^4$ Jy (Zhou et al. 2002), the maser could be detected at a position with angular distance of 5.4 HPBWs ($\sim 12'$) away above an rms of 0.17 Jy. But for most of the masers in our detection, their flux densities are a few Jy, and the corresponding influence radius is just 1.2 HPBWs ($\sim 167''$) for masers with a peak flux of 5 Jy. We used this formula to estimate the influence radius. A weak maser with a similar line profile within the influence radius of the strongest maser is considered to be a fake detection.

5.2 Comparison between Our Sample Sources in v1.0.1 and Their Counterparts in v2.1

We selected our sample sources from the BGPS catalog v1.0.1 and began the H_2O maser survey in August 2012. The BGPS catalog v2.0 was released near the end of our observations, which provided more reliable coordinates and flux densities for sources. The latest BGPS catalog version is v2.1. Since the 1.1 mm flux density within an aperture of $120''$ is used for further analysis in this paper, we compare the flux density with an aperture of $120''$ from our sample sources in v1.0.1 and that of their counterparts in v2.1. Only 70% of the individual sources in v2.1 have an obvious v1.0.1 counterpart and vice versa (Ginsburg et al. 2013), so a portion of our sources in BGPS catalog v1.0.1 may have no counterparts in v2.1. When the angular distance between any two sources coming from v1.0.1 and v2.1 respectively is less than $67.5''$ (half of the HPBW of Nanshan 25 m), they are considered to be the same source. As a result, 188 out of 274 sources in our sample have counterparts in v2.1. We plot their 1.1 mm flux densities in v1.0.1 versus those in v2.1 in Figure 4. The former have been corrected by multiplying a factor of 1.5 which is applied in flux densities of v1.0.1. The dashed line represents the equality line. It clearly shows that all of the sources are around the equality line. Hence there is no systemic deviation between catalog v1.0.1 and v2.1. So, using flux densities of our sources in catalog v1.0.1 is reasonable. Because the other 86 out of 274 sources ($\sim 30\%$) of our sample do not have their counterparts in v2.1, we use the parameters listed in the BGPS catalog v1.0.1 in further analysis below.

5.3 Classification of BGPS Sources

The Wide-field Infrared Survey Explorer (WISE) (Wright et al. 2010; Jarrett et al. 2011) is a NASA medium-class Explorer mission that was launched on 2009 December 14. WISE mapped the whole sky simultaneously in four infrared (IR) bands centered at 3.4, 4.6, 12 and 22 µm. The flux density at 5σ are 0.08, 0.1, 1 and 6 mJy respectively. WISE All-Sky Source catalog[6] was used for exploring the IR emission of BGPS sources. The WISE point sources

[6] *http://irsa.ipac.caltech.edu/cgi-bin/Gator/nph-dd*

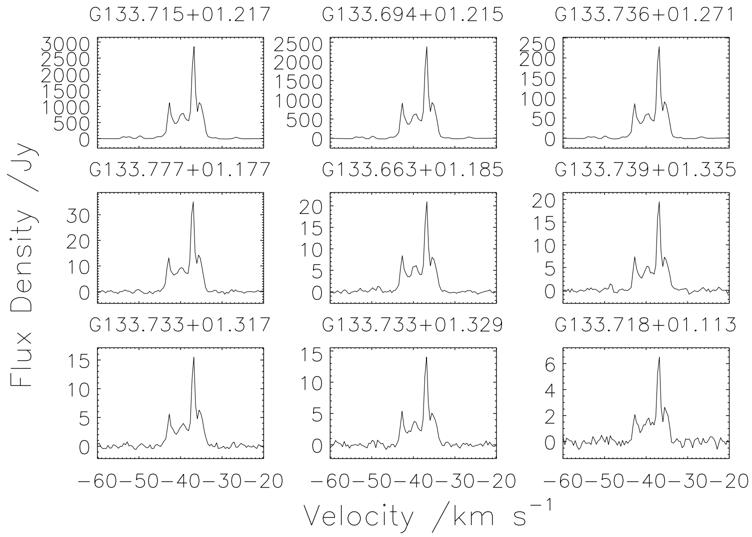

Fig. 2 Nine spectra with the same line profile but detected at different positions are shown in the figure. The BGPS name of the position is listed above each spectrum.

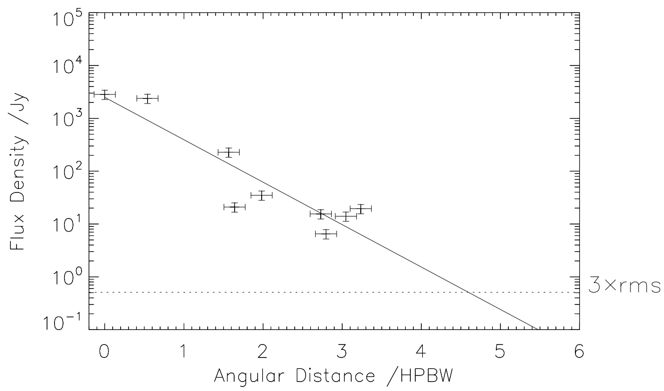

Fig. 3 The peak flux density in nine spectra is plotted as a function of angular distance. The flux density is in log-scale and the angular distance is the unit of HPBW. The solid line represents the best fitting linear line. The dotted line represents 3× the average rms in our detection.

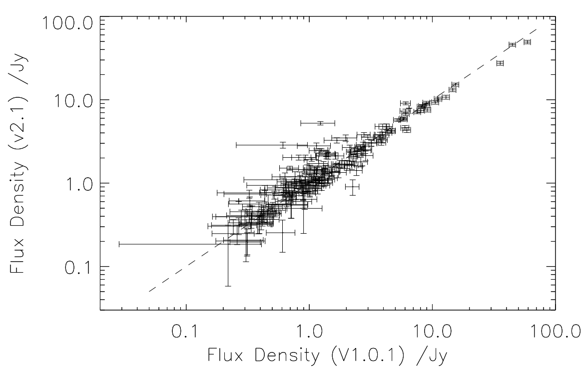

Fig. 4 A comparison of flux density with an aperture of 120″ between the BGPS catalog v1.0.1 and v2.1. The correction factor of 1.5 is applied in flux density of v1.0.1. The dashed line represents the equality line.

classified as extragalactic objects by Koenig et al. (2012) are eliminated in our further analysis.

Using data from 0.00, 0.00, 1.00 in the WISE survey, Anderson et al. (2014) compiled a catalog of $\sim$8000 Galactic HII regions and HII region candidates by their characteristic mid-IR (MIR) morphology. Also, $\sim$1500 cataloged sources with a radio recombination line (RRL) or detected H_α emission are known to be HII regions. Their work provided us with a complete and reliable HII region catalog that we have used to select the BGPS sources containing relatively evolved massive stars.

The goal of the Red MSX Source (RMS) survey[7] is to systematically search the entire Galaxy for massive young stellar objects (MYSOs) (Hoare et al. 2004; Urquhart et al. 2008). The target sources are mid-IR bright point sources that are selected from the Midcourse Space Experiment (MSX) Galactic plane survey (Price et al. 2001). The RMS survey identified 1992 MYSO candidates which are classified into the following categories: "Evolved star", "PN", "OH/IR star", "Young/old star?", "HII regions", "HII/YSO" and "YSO". We only use the "Young/old star?", "HII regions", "HII/YSO" and "YSO" as the signature of a relatively evolved massive star and marked those objects as young RMS.

The sources provided in the three catalogs described above were used to classify 274 BGPS sources in our sample. HII regions, young RMS sources and WISE point sources were considered to be associated with the BGPS sources, if they were in the elliptical region of BGPS sources provided in the catalog v1.0. Table 1 shows the result of whether a BGPS source is associated with WISE point sources, HII regions or RMS sources. The BGPS sources associated with at least one HII region or at least one young RMS source are classified as Phase 3. The BGPS sources which are not associated with any HII region or any young RMS source but are associated with at least one WISE point source are classified as Phase 2. The sources which are not associated with any HII region, young RMS source or WISE point source are classified as Phase 1. We use this classification scheme as the evolutionary stage of BGPS sources. The classification result is also shown in Table 1. As a result, there are 67, 169 and 38 BGPS sources in Phases 1, 2 and 3 respectively. The distributions of 1.1 mm flux densities for Phase 1, 2 and 3 sources are shown in Figure 5. The mean flux densities are 0.55, 1.1 and 5.2 Jy respectively which are represented by dotted lines. These clearly show that the mean flux density is increasing as the BGPS sources evolve from Phases 1 to 3. The trend is similar to that shown in Dunham et al. (2011). We use this classification in further analysis in this paper.

5.4 Detection Rate of H_2O Masers

In Figure 6, we plot the number of BGPS sources associated with and without an H_2O maser as a function of the 1.1 mm flux density of BGPS sources with an aperture of 120″. The detection rates in each bin are shown as triangles. They clearly show that the detection rate of an H_2O maser increases as the 1.1 mm flux density increases. Chen et al. (2012) also found that the detection rate of 95 GHz Class I methanol masers towards BGPS sources significantly increases as the integrated 1.1 mm flux density increase. The same trend was also found for 6.7 GHz Class II methanol masers (Sun et al. 2014). This shows that Class I and II CH_3OH masers, and H_2O masers are closely related to the 1.1 mm emission of BGPS sources. Chen et al. (2012) developed a criterion based on 1.1 mm integrated flux density of BGPS sources to search for Class I CH_3OH masers. Hence, a similar criterion could be developed to search for H_2O masers toward BGPS sources. However, the sample of H_2O masers is too small to do so in this paper.

Table 3 H_2O Maser Detection Rates in Phases 1, 2 and 3

	Phase 1	Phase 2	Phase 3
Maser	2(3.0%)	11(6.5%)	12(31.6%)
Total	67	169	38

The number of BGPS sources with and without H_2O masers in Phases 1, 2 and 3 and corresponding detection rates are listed in Table 3. The detection rates in Phases 1, 2 and 3 are 3%, 7% and 32%, respectively. The detection rates escalate from Phases 1 to 3. The detection rate in Phase 3 is much higher than that in Phases 1 and 2. However, the detection rates for Phases 1 and 2 are similar to each other. The BGPS sources in Phase 1 are not associated with HII regions, RMS sources or WISE point sources. Hence, the sources in Phase 1 have no or have weak star formation activity. The only two sources in Phase 1 are $H_2O-5632$ G111.796+00.600 and $H_2O-5726$ G137.067+03.004. One of them is a new detection, and neither maser has a position measured from high resolution observation. Further observation is needed for these two H_2O masers to confirm the association with the BGPS sources. Considering the possibility stated above, the detection rate in Phase 1 may drop. The difference in detection rate between Phases 1 and 2 may become more obvious. This escalation trend in detection rate from Phases 1 to 3 shows that the H_2O maser prefers the relatively evolved stars. As the H_2O masers are pumped by collision, intense star formation activities such as outflows and jets may provide ideal conditions for exciting H_2O masers.

Shirley et al. (2013) performed observations of HCO^+ and N_2H^+ simultaneously toward BGPS sources. Their target catalog contains all of the sources in our sample. Their detection results of HCO^+ are shown in Table 1. There are 191 sources showing HCO^+ emission and 83 sources in which Shirley et al. (2013) did not detect HCO^+ emission under the mean limit of 0.174 K. Compared with our H_2O maser sample, we found that 24 out of 25 H_2O masers we detected are among the 191 sources which are associated with HCO^+ emission. One out of 25 H_2O

[7] *http://www.ast.leeds.ac.uk/RMS/*

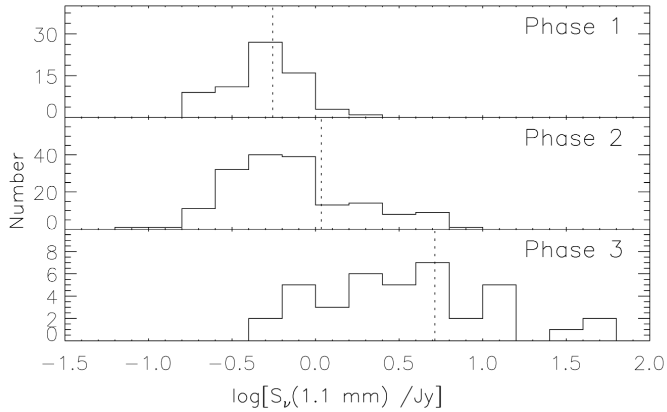

Fig. 5 This figure shows the distribution of 1.1 mm flux density in each phase. The dotted line represents the mean 1.1 mm flux density in the phase.

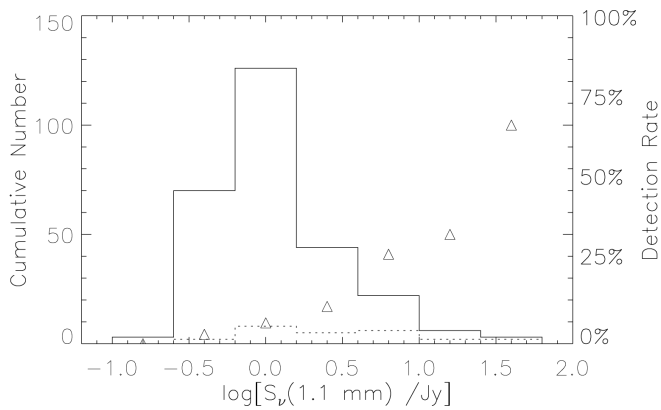

Fig. 6 This figure shows the distribution of 1.1 mm flux density of BGPS sources with an aperture of 120″. The solid line represents the BGPS sources in our sample and the dotted line represents the BGPS sources associated with H_2O masers. The detection rate of the H_2O maser in each bin is represented by a triangle.

masers was associated with a source which did not show HCO^+ emission with an rms under 0.08 K. This implies that the H_2O masers preferentially appear in the sources with HCO^+ emission. The mean T_{mb}^{pk} and median T_{mb}^{pk} are 3.126 K and 2.928 K respectively for the sources with H_2O masers. The mean T_{mb}^{pk} and median T_{mb}^{pk} are 0.938 K and 0.621 K respectively for the sources without H_2O masers. Both mean and median T_{mb}^{pk} show the trend that H_2O masers prefer to appear in the sources not only with HCO^+ emission but also with stronger HCO^+ emission. Hogerheijde et al. (1998) revealed that the emission of HCO^+ was dominated by outflow motion, and H_2O masers also trace outflows (Sanna et al. 2010a,b). This seems to be the reason why the H_2O masers we detected are associated with the sources showing stronger HCO^+ emission. This trend also provides us with a method of source selection to search for H_2O masers.

5.5 Spatial Distribution of H_2O Masers

The spatial distribution of BGPS sources in our sample is shown in the upper panel of Figure 7. The grey dots represent the BGPS sources without H_2O masers. The BGPS sources associated with H_2O masers are plotted as diamonds. The small, medium and large diamonds represent the maser sources in Phases 1, 2 and 3, respectively. Our sources are concentrated in a few regions, and it is hard to determine whether the detection rate of H_2O masers varies as the longitude increases. We divided the sources into three portions (part 1: $80° < l < 120°$, part 2: $120° < l < 160°$, part 3: $160° < l < 200°$). The detection rate of H_2O masers is 7.1%, 10.4% and 10.9% in parts 1, 2 and 3, respectively. The nearly constant detection rates of H_2O masers suggest that star formation is not correlated with Galactic longitude in the outer Galaxy. Dunham (2012) performed an H_2O maser survey towards BGPS sources, and yielded a detection rate of 40%. Another H_2O maser survey towards BGPS sources performed by Xi et al. (2015) also gave a detection rate as high as 48.4%. Compared with the previous H_2O maser survey towards BGPS sources, the detection rate in our survey is rather low. The source selection may be attributed to low detection. Another possible reason may be that star formation in the outer Galaxy is much weaker.

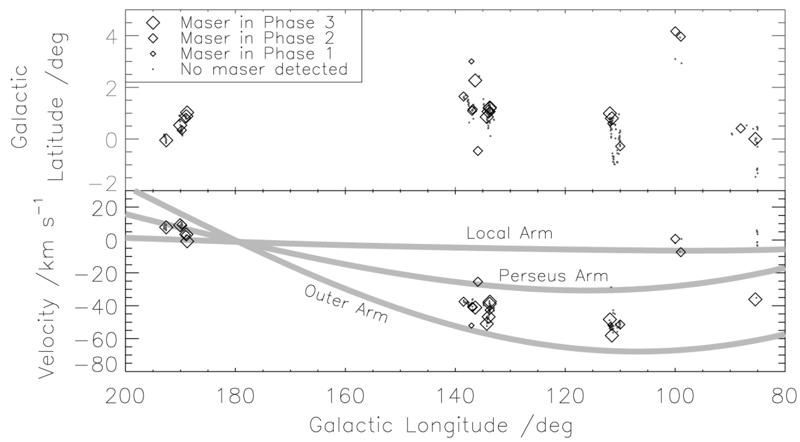

Fig. 7 The positions of BGPS sources in our sample are plotted in the upper panel. The lower panel shows the systematic velocity versus Galactic longitude of BGPS sources in our sample. The sources without H_2O masers are shown by grey dots. The H_2O masers within BGPS sources in Phases 1 to 3 are represented by small, medium and large diamonds respectively.

200 BGPS sources have known systematic velocity derived from N_2H^+ or ^{12}CO. H_2O masers were detected toward 24 of these 200 sources. We show the distribution of systematic velocity as a function of the Galactic longitude of the BGPS sources in the lower panel of Figure 7. The legend in the upper panel in Figure 7 still applies in the lower panel. Three spiral arms (Local Arm, Perseus Arm and Outer arm which are derived from a polynomial-logarithmic model fitting to only the HII region by Hou & Han (2014)) of the Galaxy in the second quadrant are shown in the lower panel. It clearly shows that most H_2O masers are located between the Perseus Arm and Outer arm, rather than in the spiral arms. We note that the H_2O masers in the gap between spiral arms contain seven H_2O masers in Phase 3. This distribution suggests that there exists a new region which is undergoing massive star formation. Hou & Han (2014) built a four-arm model based on the distribution of HII regions, giant molecular clouds and masers. The best fitting result shows the possible existence of another spiral arm between the Perseus Arm and the Outer Arm. The seven H_2O masers in Phase 3 may be located in the possible spiral arm predicted by Hou & Han (2014). The other four H_2O masers in Phase 3 are located around the longitude of 190°. The known spiral arms are near each other. It is hard to distinguish in which arm they are located. The H_2O masers in Phase 2 around a longitude of 100° are located in the Local Arm.

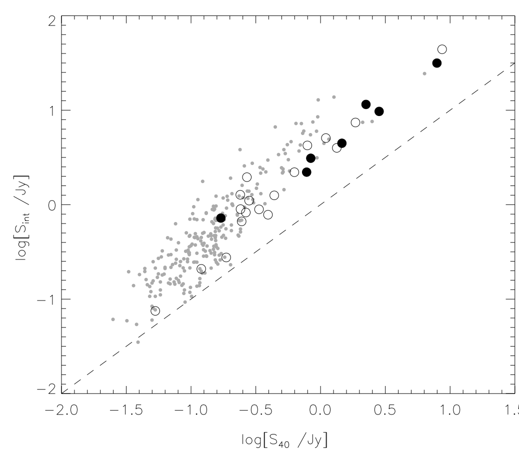

Fig. 8 The integrated flux density of BGPS sources versus the flux density within an aperture of 40″. The BGPS sources without H_2O masers are plotted with grey dots. The BGPS sources with only H_2O masers are plotted with empty circles and the BGPS sources with both H_2O and CH_3OH masers are plotted with filled circles.

5.6 1.1 mm Emission from BGPS Sources

In Figure 8, we plot the integrated flux density of BGPS sources versus the flux density within an aperture of 40″ of BGPS sources. The grey dots represent the BGPS sources without H_2O masers. The empty circles represent the BGPS sources with only H_2O masers. We check the association with the 6.7 GHz CH_3OH maser in previous work (Ellingsen 2007; Pandian et al. 2007; Xu et al. 2008; Caswell 2009; Green et al. 2010; Szymczak et al. 2012; Bayandina et al. 2012). Seven BGPS sources associated with both H_2O and CH_3OH masers are represented by filled circles. It clearly shows that the BGPS sources associated with masers tend to have higher integrated flux density and flux density within an aperture of 40″, and so tend to have a higher mass. The flux density within an aperture of 40″ accounts for most of the integrated flux density in the BGPS sources associated with masers, and so these sources tend to be more compact. This trend was also shown in Titmarsh et al. (2014). It also appears that the BGPS sources associated with both H_2O and CH_3OH masers are more compact than those only associated with an H_2O maser. More matter is accreted onto the protostar as the clump evolves. This implies the more compact sources may be relatively older. Hence, the BGPS

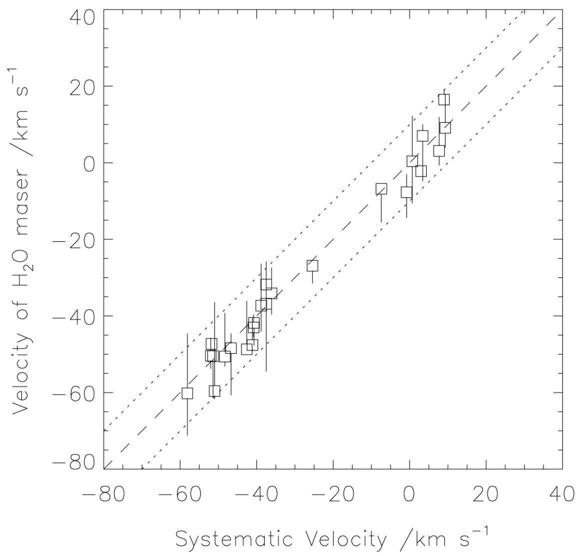

Fig. 9 The peak velocities of the H_2O maser versus the systematic velocities are plotted by squares. The vertical bars represent the total velocity ranges of H_2O masers. The dashed line represents equality. The dotted lines show a deviation of ± 10 km s^{-1} from the dashed line.

sources associated with both H_2O and CH_3OH masers may be older than those only associated with H_2O masers. Titmarsh et al. (2014) performed a similar comparison and suggested that the BGPS sources associated with both H_2O and CH_3OH masers may be older than those only associated with CH_3OH masers. Combining these two results, we suggest that the BGPS sources associated with both H_2O and CH_3OH masers may be older than those associated with either only H_2O or only CH_3OH masers.

5.7 Velocities of H_2O Masers

24 out of 25 H_2O masers have systematic velocity derived from N_2H^+ or ^{12}CO. We plotted the velocity of H_2O masers versus the systematic velocity in Figure 9. The squares show the peak velocity of H_2O masers. The vertical bars show the total velocity ranges of H_2O masers. The dashed line represents equality and the dotted lines represent a deviation of ± 10 km s^{-1} from the dashed line. The peak velocities of H_2O masers in our sample all lie within ± 10 km s^{-1} from systematic velocities. This confirms association between H_2O masers and BGPS sources. We also found that there is no high velocity emission shown in our sample, if we use the a threshold of a 30 km s^{-1} deviation from systematic velocity. But 28% of H_2O masers show high velocity emission in Caswell & Breen (2010) based on a sample of 32 H_2O masers, if we use the same criterion. There are 19% of H_2O masers showing high velocity emission in Caswell & Breen (2010), if a stronger criterion of 50 km s^{-1} is used.

The average velocity range of H_2O masers in our sample is 8.5 km s^{-1}, and the median velocity range is 7.9 km s^{-1}. Breen et al. (2010a) performed a survey of H_2O masers. The average and median velocity ranges are 27 km s^{-1} and 15 km s^{-1} for the 2003 epoch, and 30 km s^{-1} and 15 km s^{-1} for the 2004 epoch respectively. Their results were based on the sample of 379 H_2O masers. Titmarsh et al. (2014) gave a similar average and median velocity range of 27 km s^{-1} and 17 km s^{-1} respectively.

This clearly shows that the deviation of H_2O maser features from systematic velocity in our sample is much smaller than that shown in previous works. The velocity ranges in our sample are also smaller. The rms varies from ~40 to ~50 mJy in Breen et al. (2010a), and the rms varies from ~40 to ~80 mJy or from ~100 to ~160 mJy depending on integration time in Titmarsh et al. (2014). The rms in Breen et al. (2010a) and Titmarsh et al. (2014) is lower than or just a fourth of the rms in our observation. This makes them able to detect more weak features of H_2O masers. Since the features of H_2O masers with high velocities have relatively low intensities, the high velocity features are the missed ones in our observations. This may be the most probable reason why the velocity range is narrow and there is no high velocity feature detected in our observations. Another possible reason may be our biased source selection. The sources in our sample are located in the outer Galaxy, which may indicate that the conditions of SFR in the outer Galaxy differ from those in the inner Galaxy.

5.8 Flux Density and Luminosity of H_2O Masers

In Figure 10, we show the distribution of peak flux density (left panel) and luminosity (right panel) of H_2O masers in our sample from Phases 1 to 3. Considering that there are only two H_2O masers in Phase 1, which cannot give a statistically reliable result, we only analyze the variation of peak flux and luminosity of H_2O masers in Phases 2 and 3. There are 11 and 12 sources in Phases 1 and 2 respectively in the distribution of peak flux density. We calculate the luminosity for the H_2O masers which have measured distances, and there are 10 and 12 sources in Phases 1 and 2 respectively in the distribution of luminosity. The vertical bars represent the average value in each phase. The median peak flux is 5.6 Jy and 24 Jy in Phases 2 and 3, respectively. The average peak flux is 9.9 Jy and 3.4×10^2 Jy in Phases 2 and 3, respectively. Both average peak flux and median peak flux show an increment as the sources evolve. We also note that there is a large overlap in flux density of H_2O masers between Phases 2 and 3. Breen et al. (2010a) suggested that the flux density of H_2O masers increases with age, and our result is consistent with their prediction. However, the K-S test gave a p value of 0.20 which suggested there is no significant difference in peak fluxes between Phases 2 and 3. This may be caused by the small size of our sample.

We also performed the K-S test for luminosity of Phases 2 and 3. The test gave a p value of 0.04 which suggested a significant difference in luminosity between Phases 2 and 3. The average luminosity is

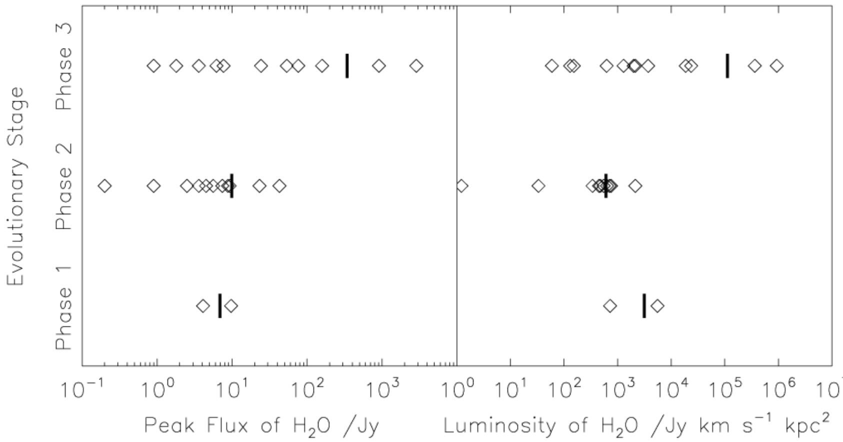

Fig. 10 The peak flux (*left panel*) and the luminosity (*right panel*) of H_2O masers in our sample versus the evolutionary stage from Phases 1 to 3. The vertical bars represent the average value in each phase.

6.0×10^2 Jy km s^{-1} kpc^2 and 1.1×10^5 Jy km s^{-1} kpc^2 in Phases 2 and 3, respectively. The median luminosity is 5.5×10^2 Jy km s^{-1} kpc^2 and 2.1×10^3 Jy km s^{-1} kpc^2 in Phases 2 and 3, respectively. This suggests that the luminosity increases as the sources evolve. There is an overlap in luminosity between Phases 2 and 3 as well as in flux density. The H_2O masers with luminosity higher than 10^4 Jy km s^{-1} kpc^2 only appear in Phase 3. This implies that the high luminosity H_2O masers may only be excited by relatively evolved sources. Breen et al. (2010b); Breen & Ellingsen (2011) also found that the luminosity of CH_3OH masers increases as they evolved.

6 CONCLUSIONS

We performed an H_2O maser survey toward 274 BGPS sources with $85° < l < 193°$ using the Nanshan 25 m radio telescope. We detected 25 H_2O masers, and five of them are new detections. The total detection rate (9%) is much lower than that of previous H_2O maser surveys targeted towards BGPS sources.

The detection rate of H_2O masers increases as the 1.1 mm flux densities of BGPS sources increase; both peak flux density and luminosity of H_2O masers increase as the sources evolve. The detection rate of H_2O masers toward BGPS sources without HCO^+ emission is low. These findings are helpful for selecting target sources for future H_2O maser searches.

The strongest H_2O maser source G133.715+01.217, which has a flux density of 2.9×10^3 Jy, was detected at eight different nearby positions. By fitting the correlation between the flux densities of these H_2O masers and their angular distances, we get the influence radius $r = \frac{1}{0.8}\log(\frac{F_0}{3\mathrm{rms}})$ for our observation. Here F_0 is the flux density of the H_2O maser, r is the angular distance to the H_2O maser in the unit of HPBW, and rms is the sensitivity of observation. The strong maser could be detected anywhere within the radius.

The BGPS sources associated with both H_2O and CH_3OH masers seem to be more compact than those only associated with H_2O masers. This indicates that the former sources may be relatively older than the latter sources. This trend is also shown in a large sample in Titmarsh et al. (2014).

Acknowledgements This work was funded by the National Natural Science Foundation of China under grant 11373062 and partly supported by the National Basic Research Program of China (973 program, 2012CB821802) and the National Natural Science Foundation of China under grant Nos. 11433008, 11303081 and 10873025, and the Program of the Light in China's Western Region (LCRW) under grant Nos. RCPY201202 and XBBS-2014-24. This work is based on observations made with the Nanshan 25 m radio telescope, which is operated by the Key Laboratory of Radio Astronomy, Chinese Academy of Sciences.

References

Aguirre, J. E., Ginsburg, A. G., Dunham, M. K., et al. 2011, ApJS, 192, 4
Anderson, L. D., Bania, T. M., Balser, D. S., et al. 2014, ApJS, 212, 1
Bae, J.-H., Kim, K.-T., Youn, S.-Y., et al. 2011, ApJS, 196, 21
Bayandina, O. S., Val'tts, I. E., & Larionov, G. M. 2012, Astronomy Reports, 56, 553
Breen, S. L., Caswell, J. L., Ellingsen, S. P., & Phillips, C. J. 2010a, MNRAS, 406, 1487
Breen, S. L., & Ellingsen, S. P. 2011, MNRAS, 416, 178
Breen, S. L., Ellingsen, S. P., Caswell, J. L., & Lewis, B. E. 2010b, MNRAS, 401, 2219
Caswell, J. L. 2007, in IAU Symposium, 242, eds. J. M. Chapman & W. A. Baan, 194
Caswell, J. L. 2009, PASA, 26, 454

Caswell, J. L., & Breen, S. L. 2010, MNRAS, 407, 2599
Chen, X., Ellingsen, S. P., He, J.-H., et al. 2012, ApJS, 200, 5
Dunham, M. K. 2012, in IAU Symposium, 287, eds. R. S. Booth, W. H. T. Vlemmings, & E. M. L. Humphreys, 286
Dunham, M. K., Robitaille, T. P., Evans, II, N. J., et al. 2011, ApJ, 731, 90
Dunham, M. K., Rosolowsky, E., Evans, II, N. J., et al. 2010, ApJ, 717, 1157
Ellingsen, S. P. 2007, MNRAS, 377, 571
Ginsburg, A., Glenn, J., Rosolowsky, E., et al. 2013, ApJS, 208, 14
Green, J. A., Caswell, J. L., Fuller, G. A., et al. 2010, MNRAS, 409, 913
Hachisuka, K., Brunthaler, A., Menten, K. M., et al. 2006, ApJ, 645, 337
Han, F., Mao, R. Q., Lu, J., et al. 1998, A&AS, 127, 181
Hoare, M. G., Lumsden, S. L., Oudmaijer, R. D., et al. 2004, in Astronomical Society of the Pacific Conference Series, 317, Milky Way Surveys: The Structure and Evolution of our Galaxy, eds. D. Clemens, R. Shah, & T. Brainerd, 156
Hogerheijde, M. R., van Dishoeck, E. F., Blake, G. A., & van Langevelde, H. J. 1998, ApJ, 502, 315
Hou, L. G., & Han, J. L. 2014, A&A, 569, A125
Jarrett, T. H., Cohen, M., Masci, F., et al. 2011, ApJ, 735, 112
Kennicutt, R. C. 2005, in IAU Symposium, 227, Massive Star Birth: A Crossroads of Astrophysics, eds. R. Cesaroni, M. Felli, E. Churchwell, & M. Walmsley, 3
Koenig, X. P., Leisawitz, D. T., Benford, D. J., et al. 2012, ApJ, 744, 130
Moscadelli, L., Sanna, A., & Goddi, C. 2011, A&A, 536, A38
Pandian, J. D., Goldsmith, P. F., & Deshpande, A. A. 2007, ApJ, 656, 255
Price, S. D., Egan, M. P., Carey, S. J., Mizuno, D. R., & Kuchar, T. A. 2001, AJ, 121, 2819
Rosolowsky, E., Dunham, M. K., Ginsburg, A., et al. 2010, ApJS, 188, 123
Sanna, A., Moscadelli, L., Cesaroni, R., et al. 2010a, A&A, 517, A71
Sanna, A., Moscadelli, L., Cesaroni, R., et al. 2010b, A&A, 517, A78
Schlingman, W. M., Shirley, Y. L., Schenk, D. E., et al. 2011, ApJS, 195, 14
Shirley, Y. L., Ellsworth-Bowers, T. P., Svoboda, B., et al. 2013, ApJS, 209, 2
Sun, Y., Xu, Y., Chen, X., et al. 2014, A&A, 563, A130
Sunada, K., Nakazato, T., Ikeda, N., et al. 2007, PASJ, 59, 1185
Surcis, G., Vlemmings, W. H. T., Curiel, S., et al. 2011, A&A, 527, A48
Szymczak, M., Wolak, P., Bartkiewicz, A., & Borkowski, K. M. 2012, Astronomische Nachrichten, 333, 634
Titmarsh, A. M., Ellingsen, S. P., Breen, S. L., Caswell, J. L., & Voronkov, M. A. 2014, MNRAS, 443, 2923
Urquhart, J. S., Hoare, M. G., Lumsden, S. L., Oudmaijer, R. D., & Moore, T. J. T. 2008, in Astronomical Society of the Pacific Conference Series, 387, Massive Star Formation: Observations Confront Theory, eds. H. Beuther, H. Linz, & T. Henning, 381
Urquhart, J. S., Morgan, L. K., Figura, C. C., et al. 2011, MNRAS, 418, 1689
Valdettaro, R., Palla, F., Brand, J., et al. 2001, A&A, 368, 845
Wouterloot, J. G. A., & Walmsley, C. M. 1986, A&A, 168, 237
Wright, E. L., Eisenhardt, P. R. M., Mainzer, A. K., et al. 2010, AJ, 140, 1868
Xi, H., Zhou, J., Esimbek, J., et al. 2015, MNRAS, 453, 4203
Xiang, D., & Turner, B. E. 1995, ApJS, 99, 121
Xu, Y., Li, J. J., Hachisuka, K., et al. 2008, A&A, 485, 729
Zhou, J. J., Zheng, X. W., & Chen, Y. X. 2002, A&A, 390, 281
Zinneker, H. 1990, in Astrophysics and Space Science Library, 162, Physical Processes in Fragmentation and Star Formation, eds. R. Capuzzo-Dolcetta, C. Chiosi, & A. di Fazio, 201